

ρ^0 meson from two-flavor dynamical domain wall fermions

Koichi Hashimoto^{1,2}; and Taku Izubuchi^{1,3};

(for the RBC collaboration)

¹Institute for Theoretical Physics, Kanazawa University, Kakumae,
Kanazawa 920-1192, Japan

²Radiation Laboratory, RIKEN, Wako, Saitama 351-0198, Japan

³RIKEN-BNL Research Center, Brookhaven National Laboratory, Upton,
NY 11973, USA

Abstract

We explore flavor singlet pseudoscalar meson, ρ^0 , spectrum in two-flavor ($N_f = 2$) lattice QCD. The continuum-like relation between the topology of the QCD vacuum and the $U(1)_A$ anomaly, that prevents ρ^0 meson from being a would-be Nambu-Goldstone boson, are expected to hold in the domain wall fermions (DWF) used as a lattice quark field in this work. Although our simulation is limited to relatively heavy quark masses and statistical error is not magnificently small despite of improvements in measurements and fitting procedures for meson propagators, we obtained $m_{\rho^0} = 819(127)$ MeV for $N_f = 2$ QCD, where the error is statistical only. Potentially serious systematic error in the number are discussed. Results for other meson are also reported.

x1. Introduction

One of the most fascinating puzzles in the meson mass spectrum is the one called $U(1)_A$ problem: why the mass of flavor singlet pseudoscalar meson, η' is so heavier, $m_{\eta'} = 957.78(14)$ MeV than that of flavor non-singlet counterparts, $m_{\eta} = 134.9766(6)$ MeV, $m_{K^0} = 497.648(22)$ MeV, and $m_{\pi} = 547.51(18)$ MeV in nature.¹⁾

Non-singlet mesons behave as Nambu-Goldstone (NG) bosons of spontaneous breaking of $SU(3)_A$ symmetry in quark massless limit ($m_{\text{quark}} \rightarrow 0$) ignoring the small QED effects while η' is not a NG boson because $U(1)_A$ symmetry is broken by the quantum effect, $U(1)_A$ anomaly. The non-vanishing divergence of the flavor singlet axial current, $A^0(x)$ in the axial Ward-Takahashi identity (AWTI) for an operator O in the degenerate quarks case upto the contact term,

$$\partial_\mu A^b(x)O = 2m_{\text{quark}} P^a(x)O + \frac{1}{f^2} 2N_f \text{top}(x)O; \quad (1.1)$$

expresses the anomalous breaking of chiral symmetry as the last term, which is proportional to the topological charge density, $\text{top}(x)$. For sufficiently smooth gauge field,

$$\text{top}(x) = \frac{1}{32\pi^2} \text{tr} F \wedge F(x); \quad (1.2)$$

The difference of pseudoscalar meson masses between the flavor singlet sector, $m_{\eta'}$, and the non-singlet sector, m_{η} , was estimated by the Witten-Veneziano (WV) relation,^{2),3)}

$$m_{\eta'}^2 - m_{\eta}^2 = \frac{2N_f}{f^2} \chi_{\text{top}} \quad (1.3)$$

in $N_c \rightarrow \infty$ limit, where χ_{top} is the topological charge susceptibility

$$\chi_{\text{top}} = \frac{Q_{\text{top}}^2}{VT}; \quad Q_{\text{top}} = \int_{\text{top}} \text{top}(x) d^4x; \quad (1.4)$$

in pure Yang-Mills (YM) theory on a four dimensional volume, VT . Recent result in $N_c = 3$ YM theory with overlap fermion⁴⁾ shows $\chi_{\text{top}} = (191(5)\text{MeV})^4$. η' mass from this estimation for $N_f = 3$ and in the chiral limit, ($m^2 \rightarrow 0$), is $m_{\eta'} = 970$ MeV which is very close to experimental values.

The direct numerical calculation for η' spectrum is important to check the theoretical scenarios such as WV relation, and should provide its correction in finite N_c and non-zero quark masses.

The simulations of η' physics in pure Yang-Mills (YM) theory with quenched Wilson fermions were carried out in pioneer works.^{5),6)} The relation between topological charge and

π_0 mass was also explored.⁷⁾ Unquenched simulations⁸⁾⁽¹²⁾ were done for two-flavors and for 2+1 flavors¹³⁾ of Wilson fermions. Using the staggered fermions, m_{π_0} is calculated for $N_f = 0; 2$ ¹⁴⁾ and $N_f = 2 + 1$.^{46),47)} Recently there are other interesting explorations, such as using twisted mass quarks⁴⁸⁾ or an imaginary γ_5 -term.⁴⁹⁾

In this paper, we discuss π_0 mass in $N_f = 2$ QCD with domain wall fermions (DWF). DWF¹⁸⁾⁽²⁰⁾ is one of lattice chiral fermion, which has both flavor and chiral symmetries even at finite lattice spacing ($a > 0$), and thus suitable to investigate non-perturbative physics of chiral anomaly. These features of DWF are preferable to the other alternative discretization. Wilson fermions break chiral symmetry at $a > 0$ and discretization errors would start at $O(a^2)$ (a_{QCD}). The singlet flavor meson in staggered fermions is very important subject as it may be related to the potential issue about the locality of the formalism in the continuum limit.^{16),17)}

Chiral and flavor symmetry is especially important for π_0 physics, and DWF is the natural choice of lattice quark. Chiral symmetry in DWF is not realized perfectly, it is broken due to its finite extent in the fifth direction, L_s . The amount of breaking could be measured by a shift in quark mass: $m_{\text{quark}} = m_f + m_{\text{res}}$, so that the non-singlet axial current is conserved at $m_{\text{quark}} = 0$. m_{res} is called residual quark mass and will vanish at large L_s for sufficiently smooth gauge configuration.

Although it will be desirable to take $L_s \rightarrow \infty$ limit, we restrict ourselves to finite $L_s = 12$ with the combination of DBW2 improved gauge action,^{21),22)} which smoothen gauge field at short distance and reduces m_{res} significantly.²³⁾

The RBC Collaboration examined the first large scale dynamical DWF simulation.²⁴⁾ Pseudoscalar meson masses and decay constants are computed and fit to the chiral perturbation theory (ChPT) formula. $m_\pi, m_K, m_\eta, f_\pi$ and f_K calculated in their work are somewhat consistent with those in experiments. J parameter is closer to phenomenological value than quenched simulation. Non-singlet scalar meson, a_0 , mass and decay constant are also examined both in dynamical QCD and partially quenched QCD using partially quenched ChPT.²⁵⁾

We will mainly focus on π_0 meson in this paper, but we will also report on results of other mesons belong to other Lorentz and flavor representations, and also explore for signal of the excited state mesons and their decay constants.

As the results is limited to Isospin symmetric case and the number of the dynamical quark is two, our focal interest in this paper is to provide a benchmark calculation for general meson spectrum study on dynamical DWF ensemble with various (smearing) meson field using higher statistics than the previous study.

In Section II, the theoretical expectations about π_0 meson physics will be summarized.

We will explain details of the simulation including the improvements for the signal to noise ratio and the methods relates the simulation data to physical quantities in Section III. The numerical results are presented in Section IV with a list of their systematic uncertainties. We will summarize in Section V.

2. Theoretical expectations about physics of flavor singlet meson

In (continuum Euclidean) QCD with N_f degenerated quarks, the operator of flavor singlet pseudoscalar meson, $\phi^0: I(J^P) = 0(0^-)$, is defined by quark operators, q_f , as

$$\phi^0(x) = \frac{1}{\sqrt{N_f}} \sum_{f=1}^{N_f} q_f(x) i \gamma_5 q_f(x); \quad (2.1)$$

where $f = 1; \dots; N_f$ is flavor index. ϕ^0 propagator is consists of two parts:

$$\begin{aligned} \int d^3x \langle \phi^0(x;t) \phi^0(0;0) \rangle &= C_\phi(t) - N_f D_\phi(t); \quad (2.2) \\ C_\phi(t) &= \int d^3x \frac{1}{N_f} \sum_f \langle \text{tr} \{ \gamma_5 q_f(x;t) \gamma_5 q_f(x;t) q_f(0;0) \} \rangle; \\ D_\phi(t) &= \int d^3x \frac{1}{N_f} \sum_f \langle \text{tr} \{ \gamma_5 q_f(x;t) \gamma_5 q_f(x;t) \} \rangle \frac{1}{N_f} \sum_g \langle \text{tr} \{ \gamma_5 q_g(0;0) \gamma_5 q_g(0;0) \} \rangle; \end{aligned}$$

The braces represents how to contract quark propagators, $S_q(0;t)$. So, for example, $C_\phi(t)$ is $\langle S_q(t;0) \gamma_5 S_q(0;t) \gamma_5 \rangle$, just same as the non-singlet meson (pion) propagator, and $D_\phi(t)$ is the correlation function between disconnected quark loops, which exists in the flavor singlet mesons. While $D_\phi(t)$ is suppressed by OZI rule, it propagates picking $U(1)_A$ anomaly.

In dynamical QCD, in which mass of quark polarizing the gluon, m_{sea} , is equal to that of quark consisted in the meson operator, m_{val} , ϕ^0 propagator shall be a exponential function in time with its damping factor being the mass of the meson, m^0 ,

$$\int d^3x \langle \phi^0(x;t) \phi^0(0;0) \rangle = C_\phi(t) - N_f D_\phi(t) = A e^{-m^0 t} + \dots; \quad (3.2)$$

at large t .

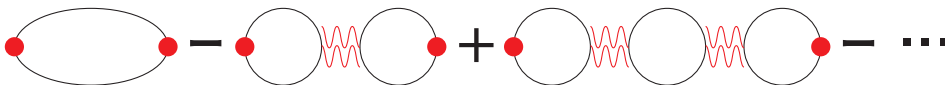


Fig. 1. Diagram of ϕ^0 propagator.

A model of the η' propagator is depicted in Figure 1. The meson propagator is expressed as an expansion in number of quark loops with signs reflecting the Grassmannian feature of the quark, and the blobs at the ends are the meson operators (2.1). The wavy lines connecting quark loops are the coupling between disconnected loops attached to the pseudo scalar density, which is related to the $U(1)_A$ anomaly.

The meson propagator in momentum space could be calculated based on the model. The first term in (1) is just same as the non-singlet pseudoscalar meson (pion), $1/(p^2 + m^2)$, and the second term would be two pion propagators coupled by gluon, $1/(p^2 + m^2) \cdot m_0^2/N_f \cdot 1/(p^2 + m^2)$, whose coupling we parameterized as m_0^2/N_f . There are N_f combinations of quark loops at the second term. Repeating the similar identification of connected pion propagators to n -th order, the momentum space representation of η' propagator could be written as a geometrical series:

$$\begin{aligned} & \langle \eta'(p) | \eta'(p) \rangle \\ & / \frac{1}{p^2 + m^2} + N_f \frac{1}{p^2 + m^2} \frac{m_0^2}{N_f} \frac{1}{p^2 + m^2} + N_f^2 \frac{1}{p^2 + m^2} \frac{m_0^2}{N_f} \frac{1}{p^2 + m^2} \frac{m_0^2}{N_f} \frac{1}{p^2 + m^2} \\ & = \frac{1}{p^2 + m^2} \sum_{n=0}^{\infty} \left(\frac{m_0^2}{p^2 + m^2} \right)^n = \frac{1}{p^2 + (m^2 + m_0^2)}; \end{aligned} \quad (2.4)$$

The pole in the connected diagram, C_5 , is exactly canceled by a part of the disconnected diagram, D_5 , and thus squared η' meson mass, $m_{\eta'}^2$, is identified by $m^2 + m_0^2$, which means η' will not behave as Nambu-Goldstone boson. In terms of this model, η' spectroscopy from lattice simulation should reveal how large m_0^2 is, and if it is consistent with the W/V relation (1.3).

In later section, we will also calculate a ratio between $D_5(t)$ and $C_5(t)$ $A e^{-m t}$. From (2.3), the ratio at large t should behave as

$$\begin{aligned} \frac{N_f D_5(t)}{C_5(t)} &= 1 - B e^{-m t} + \dots; \quad (2.5) \\ m &= m_0 - m; \quad B = \frac{A_0}{A}; \end{aligned} \quad (2.6)$$

The ratio at large t shall approach exponentially to unity with the exponent being the mass difference between the η' and pion, which is a signature of the dynamical QCD. This is in contrast to the quenched QCD, in which m_{sea} is taken to be infinitely heavy leaving m_{val} finite. In this non-unitary theory, the third and higher terms in the quark loop expansion (2.3) would be missing due to the decoupling of the sea quark, and the resulting meson propagator has unphysical double pole,

$$\langle \eta'(p) | \eta'(p) \rangle_{\text{quenched}} / \frac{1}{p^2 + m^2} + N_f \frac{1}{p^2 + m^2} \frac{m_0^2}{N_f} \frac{1}{p^2 + m^2}; \quad (2.7)$$

The ratio $D_5(t)/C_5(t)$ in this case behaves as a linear function in time coordinate,

$$\frac{N_f D_5^{(\text{quenched})}(t)}{C_5(t)} = \frac{m_0^2}{2m} t + \text{const} + \dots; \quad (3.2)$$

which is clearly different from (2.6). Thus, to obtain a physical θ we must simulate the dynamical theory ($m_{\text{sea}} = m_{\text{val}}$). We will examine the θ in domain wall QCD only at the dynamical points.

3. Simulation details

3.1. Domain wall fermion (DWF)

The DWF action is defined as

$$S_F = \sum_{x,y;s;s^0} (\bar{x};s) D_{\text{DWF}}(x;s;y;s^0) (y;s^0); \quad (3.1)$$

$$D_{\text{DWF}}(x;s;y;s^0) = D_{s;s^0}^k + D_{x;y}^?; \quad (3.2)$$

$$D_{x;y}^k = \frac{1}{2} \sum_{=1}^4 (1 - \gamma_x) U(x) \gamma_{x+\hat{y}} + (1 + \gamma_y) U^y(y) \gamma_{x-\hat{y}} + (M_5 - 4) \gamma_{xy}; \quad (3.3)$$

$$D_{s;s^0}^? = \frac{1}{2} [(1 - \gamma_s) \gamma_{s+1;s^0} + (1 + \gamma_s) \gamma_{s-1;s^0}] + \frac{m_f}{2} [(1 - \gamma_s) \gamma_{s;L_s-1;0;s^0} + (1 + \gamma_s) \gamma_{s;0;L_s-1;s^0}]; \quad (3.4)$$

where $(x;s)$ is called DWF which locates on five dimensional space $(x;s)$, L_s is size of fifth direction and the parameter M_5 is called domain wall height. By setting M_5 in a region around $[0;2]$, from (3.4), left-(right)-handed zero-modes are localized around $s = 0$; $(L_s - 1)$ and the zero-modes damp exponentially as s ; $(L_s - 1 - s)$ increase. When four dimensional fermion and anti-fermion, $q(x)$ and $\bar{q}(x)$, are defined as

$$q(x) = \frac{1 - \gamma_s}{2} (x;0) + \frac{1 + \gamma_s}{2} (x;L_s - 1); \quad (3.5)$$

$$\bar{q}(x) = (x;0) \frac{1 + \gamma_s}{2} + (x;L_s - 1) \frac{1 - \gamma_s}{2}; \quad (3.6)$$

chiral symmetry is fulfilled even with finite lattice spacing ($a > 0$) in $L_s \rightarrow \infty$ limit.

However, in actual simulation, L_s is restricted to be finite, and the AW TI is modified from the one in the continuum theory as,

$$\partial_\mu A^b(x) O = 2(m_f + m_{\text{res}}) P^b(x) O; \quad (3.7)$$

ie. the physical quark mass is shifted as $m_{\text{quark}} = m_f + m_{\text{res}}$. The m_{res} is a small lattice artifact called residual quark mass, defined as

$$m_{\text{res}} = \lim_{t \rightarrow 1} \frac{\sum_x \text{Tr} [P^D(x;t) J_{5q}^b(x;t) P^b(0;0)]}{\sum_x \text{Tr} [P^D(x;t) P^b(0;0)]} \quad (3-8)$$

where $J_{5q}^b(x;t)$ is a operator similar to pseudoscalar operator but made of fermions at midpoint of fifth direction,²⁰⁾ $s = L_s=2$, so the numerator of (3-8) includes the contractions between the surface fermions at $s = 0$ or $s = L_s$ and the midpoint fermions at $s = L_s=2$. For flavor non-singlet case, $b \neq 0$, the m_{res} is exponential function of L_s , as a consequence of the exponentially localized zero modes to the surface, and vanish in $L_s \rightarrow \infty$.

One could further argue⁵¹⁾ that the effective Lagrangian contains the diverging, $O(a)$, discretization error, which could be corrected by the small shift of quark mass, $m_{\text{quark}} = m_f + m_{\text{res}}$. The remaining error is $O(a)$ similar to that of Wilson fermions, however, it is exponentially small number, e^{-L_s} , or $O(m_{\text{res}})$. Although m_{res} is small compared to statistical errors we will have in most of observables, we will treat the shifted quark mass $m_{\text{quark}} = m_f + m_{\text{res}}$ as the physical quark mass so that our analysis is precise modulo $O(m_{\text{res}}a^2)$, which is a few percent in our simulation.

On the other hand, for flavor singlet ($b = 0$) case, $J_{5q}^b(x;t)$ in (3-8) can be attached to a quark loop without propagate in entire L_s in fifth direction, which is free from the suppression, m_{res} remains finite even in $L_s \rightarrow \infty$ and reproduce the anomalous term⁵⁰⁾

$$\sum_x \text{Tr} [J_{5q}^b(x;t) O_{b=0}(x)] \neq \sum_x \text{Tr} [J_{5q}^b(x;t) O_{\text{top}}(x)] \quad (3-9)$$

In summary, DWF even in finite L_s correctly reproduces the quantum anomaly of axial symmetry with small error due to lattice discretization.

3.2. Ensemble: Actions and Parameters

We employ $N_f = 2$ QCD ensemble²⁴⁾ with DWF actions described in previous subsection. Our gauge action is the one with an improvement in the sense of renormalization group invariance, DBW 2²²⁾

$$S_G = \frac{1}{3} \sum_{x; >} \text{ReTr} [L_P(x)] + c_1 \sum_{x; \#} \text{ReTr} [L_R(x)] \quad (3-10)$$

$$L_P(x) = U(x) U(x+\hat{\mu}) U^\dagger(x+\hat{\mu}) U^\dagger(x); \quad (3-11)$$

$$L_R(x) = U(x) U(x+\hat{\mu}) U(x+2\hat{\mu}) U^\dagger(x+\hat{\mu}+\hat{\nu}) U^\dagger(x+\hat{\nu}) U^\dagger(x); \quad (3-12)$$

with $\beta = 0.80$, $c_1 = 1.4069$. The parameters of DWF action (3-4) are set as $L_s = 12$, and $M_5 = 1.8$. We measure on 470-940 lattice configurations for each of three masses, $m_f = 0.02$,

0.03, 0.04, which corresponds to $m_{\text{res}} = 0.51\text{--}0.64$. Lattice size is $16^3 \times 32$, lattice scale is $a = 1.5 \text{ GeV}^{-1}$ ($a = 0.13 \text{ fm}$), and residual chiral breaking $m_{\text{res}} = 0.00137(4)$ which is about an order of magnitude smaller than input quark masses. Throughout this paper we estimate statistical error using the blocked Jackknife methods. The size of block is determined to be 50 trajectories by monitoring the autocorrelation of observable. The summary of Lattice ensembles and parameters are listed in Table I. For other results on these ensemble could be found in^{(24), (25), (29) (31)}

Table I. Lattice ensembles and simulation parameters.

β	V	T	$a^{-1} [\text{GeV}]$	$a [\text{fm}]$	$V a^3 [\text{fm}^3]$	m_{res}	
0.80	14069	16^3	32	1.537(26)	0.1284(22)	$(2.054)^3$	0.00137(4)
m_{f}	m_{res}	begin-end (step) traj.		# con g.	N_{noise}		
0.02	0.5121(36)	656–5351 (5)		940	1		
0.03	0.5984(31)	615–6205 (10)		560	3		
0.04	0.6415(33)	625–1765 (10), 2075–5615 (10) ^a		470	2		

(a) For the $m_{\text{f}} = 0.04$ ensemble, we do not use trajectories 1775–2065 due to a hardware error on trajectory 1772 that was not detected until lattice generation was finished.

3.3. Improvements: Smearing and Sources

Before constructing the meson propagators, we describe about improvement for the quark propagators in this section. The flavor singlet meson spectrum is known to be difficult to reduce the statistical error. As we have seen in previous section, the meson propagator includes the correlation function between disconnected loops, $D_{ij} = \langle \bar{\psi}_i \psi_j \rangle$, whose statistical fluctuation is very large, especially for large t as we will see. We have implemented the smearing for quark operator in gauge covariant manner called Wuppertal smearing.⁽²⁶⁾ The smeared quark operator q_{S}^c is a gauge covariant superposition of the local quark operator q_{L}^c :

$$q_{\text{L}}^c(\mathbf{x}; t) \equiv q_{\text{S}}^c(\mathbf{x}; t) = \sum_{\mathbf{y}; c^0} F^{c; c^0}(\mathbf{x}; \mathbf{y}) q_{\text{L}}^c(\mathbf{y}; t); \quad (3-13)$$

$$F^{c; c^0}(\mathbf{x}; \mathbf{y}) = \frac{1}{4} \left(1 + \frac{1}{4N} \sum_{i=1}^3 (r_i^x + r_i^y) \right); \quad (3-14)$$

$$[1]_{\mathbf{x}; c; \mathbf{y}; c^0} = \delta_{\mathbf{x}; \mathbf{y}} \delta_{c; c^0}; \quad (3-15)$$

$$[r_i^x]_{\mathbf{x}; c; \mathbf{y}; c^0} = U_i^x(\mathbf{x}; t) \delta_{\mathbf{x} + \hat{i}; \mathbf{y}} \delta_{c; c^0}; \quad (3-16)$$

$$[r_i^y]_{\mathbf{x}; c; \mathbf{y}; c^0} = U_i^y(\mathbf{y}; t) \delta_{\mathbf{x}} \delta_{\mathbf{y} + \hat{i}} \delta_{c; c^0}; \quad (3-17)$$

The shape of $q_{\mathbf{x}}$ in terms of $q_{\mathbf{L}}$ is Gaussian with its width $\propto 1/N$ in large N limit. We set $\beta = 4.35$ and $N = 40$. The overlap between the ground state and the meson operator made of smeared quark is expected to be larger, and the excited state contamination would be suppressed for small t , where the statistical error is smaller.

Both of quark correlation function, $C(\mathbf{x};t)$ and $D(\mathbf{x};t)$, is calculated for complex Z_2 noise source, ξ , defined by

$$\xi^{(n)}(\mathbf{x};t) = \frac{1}{\sqrt{2}} [i_1^{(n)}(\mathbf{x};t) + i_2^{(n)}(\mathbf{x};t)]; \quad (3.18)$$

where $n = 1; 2; \dots; N_{\text{noise}}$ is number of random noise ensembles and $i_1; i_2$ take ± 1 randomly. $\xi^{(n)}(\mathbf{x};t)$ is statistically independent of space-time so that it satisfies

$$\lim_{N_{\text{noise}} \rightarrow \infty} \frac{1}{N_{\text{noise}}} \sum_{n=1}^{N_{\text{noise}}} \xi^{(n)}(\mathbf{x};t) \xi^{(n)}(\mathbf{y};t^0) = 0; \quad (3.19)$$

$$\lim_{N_{\text{noise}} \rightarrow \infty} \frac{1}{N_{\text{noise}}} \sum_{n=1}^{N_{\text{noise}}} \xi^{(n)}(\mathbf{x};t) \xi^{(n)}(\mathbf{y};t^0) = \delta_{\mathbf{x}\mathbf{y}} \delta_{t,t^0}; \quad (3.20)$$

which is useful for calculating the disconnected loops as we will see in the next subsection. We use the source restricted on a time slice (wall source) for $C(\mathbf{x};t)$ and space-time volume source for $D(\mathbf{x};t)$, and $N_{\text{noise}} = 1, 3, 2$ for $m_f = 0.02, 0.03, 0.04$.

3.4. Meson Operators and Correlation Functions

Our naming convention for meson field is similar to the one used in the particle data group,¹⁾ but we note our simulation is limited to have only up and down quarks ($N_f = 2$) with degenerate masses and zero electric charges, thus the meson spectrum are inevitably different from those in the real world. Besides meson with strange quarks such as kaons, the systematic error from these omission could be comparable or smaller to our aiming precision, 10%. But this points certainly needs further investigation.

The Hermitian interpolation fields for flavor non-singlet meson in our simulation, $\rho, \omega, \pi, a_0, a_1, b_1$, and singlet fields, $\eta, \eta', f_0, f_1, h_1$ are defined in terms of quark operators, $q_{I;f}; \bar{q}_{J;f}$ as follow:

$$\rho_I(\mathbf{x};t) = \frac{1}{\sqrt{2}} \sum_{f;g=1}^2 X^2 q_{I;f}(\mathbf{x};t) \bar{q}_{f;g}(\mathbf{x};t) - \frac{1}{\sqrt{2}} \sum_{f;g=1}^2 X^2 q_{I;f}(\mathbf{x};t) \bar{q}_{g;f}(\mathbf{x};t); \quad (3.21)$$

$$\pi_I(\mathbf{x};t) = \frac{1}{\sqrt{6}} \sum_{i=1}^3 X^3 q_{I;i}(\mathbf{x};t) \bar{q}_{i;1}(\mathbf{x};t) - \frac{1}{\sqrt{6}} \sum_{i=1}^3 X^2 q_{I;i}(\mathbf{x};t) \bar{q}_{i;2}(\mathbf{x};t) + \frac{1}{\sqrt{6}} \sum_{i=1}^3 X^2 q_{I;i}(\mathbf{x};t) \bar{q}_{i;3}(\mathbf{x};t); \quad (3.22)$$

$$a_{0I}(\mathbf{x};t) = \frac{1}{\sqrt{2}} \sum_{f;g=1}^2 X^2 q_{I;f}(\mathbf{x};t) \bar{q}_{f;g}(\mathbf{x};t) + \frac{1}{\sqrt{2}} \sum_{f;g=1}^2 X^2 q_{I;f}(\mathbf{x};t) \bar{q}_{g;f}(\mathbf{x};t); \quad (3.23)$$

$$a_{1I}(\mathbf{x};t) = \frac{1}{6} \sum_{i=1}^3 \sum_{f,g=1}^3 X^3 X^2 q_{I,f}(\mathbf{x};t) b_{fg}^i i_5 q_{I,g}(\mathbf{x};t) \quad (3.24)$$

$$b_{1I}(\mathbf{x};t) = \frac{1}{6} \sum_{\substack{i,j=1 \\ i < j}}^3 \sum_{f,g=1}^3 X X^2 q_{I,f}(\mathbf{x};t) b_{fg}^i i_i q_{I,g}(\mathbf{x};t) \quad (3.25)$$

$$a_I^0(\mathbf{x};t) = \frac{1}{2} \sum_{f=1}^3 X^2 q_{I,f}(\mathbf{x};t) i_5 q_{I,f}(\mathbf{x};t); \quad (3.26)$$

$$!_I(\mathbf{x};t) = \frac{1}{6} \sum_{i=1}^3 \sum_{f=1}^3 X^3 X^2 q_{I,f}(\mathbf{x};t) i_i q_{I,f}(\mathbf{x};t) \quad (3.27)$$

$$f_{0I}(\mathbf{x};t) = \frac{1}{2} \sum_{f=1}^3 X^2 q_{I,f}(\mathbf{x};t) q_{I,f}(\mathbf{x};t); \quad (3.28)$$

$$f_{1I}(\mathbf{x};t) = \frac{1}{6} \sum_{i=1}^3 \sum_{f=1}^3 X^3 X^2 q_{I,f}(\mathbf{x};t) i_5 q_{I,f}(\mathbf{x};t) \quad (3.29)$$

$$h_{1I}(\mathbf{x};t) = \frac{1}{6} \sum_{\substack{i,j=1 \\ i < j}}^3 \sum_{f=1}^3 X X^2 q_{I,f}(\mathbf{x};t) i_i q_{I,f}(\mathbf{x};t) \quad (3.30)$$

where b^i ($b = 1;2;3$) is Pauli matrix for flavor index $f;g$, and $I;J$ is whether we use local quark field (L) or smeared one (S) to control the ground state overlap. In Table II, we summarize the quantum numbers of each meson fields.

Table II. Meson operators in the simulation and their quantum numbers.

Meson type	J^{PC}	non-singlet			singlet
pseudoscalar	0^-	i_5			0
vector	1^-	i_i^a			$!$
scalar	0^{++}	1	a_0		f_0
pseudovector	1^{+-}	$i_5 i_i^a$	a_1		f_1
pseudovector	1^+	$i_i j^a$	b_1		h_1

(a) average over $i;j = 1;2;3$ is taken.

The two point correlation functions between the interpolation fields are calculated as

$$\sum_{\mathbf{x},\mathbf{y}} h_I(\mathbf{x};t) \sum_J(\mathbf{y};0) i = C_{IJ;5}(t); \quad (3.31)$$

$$\sum_{\mathbf{x},\mathbf{y}} h_I(\mathbf{x};t) \sum_J(\mathbf{y};0) i = \frac{1}{3} \sum_{i=1}^3 C_{IJ;i}(t); \quad (3.32)$$

$$\sum_{x,y} \langle h_{0I}(\mathbf{x};t) a_{0J}^y(\mathbf{y};0) \rangle_i = C_{IJ;1}(t); \quad (3.33)$$

$$\sum_{x,y} \langle h_{1I}(\mathbf{x};t) a_{1J}^y(\mathbf{y};0) \rangle_i = \frac{1}{3} \sum_{i=1}^3 X^3 C_{IJ;5_i}(t); \quad (3.34)$$

$$\sum_{x,y} \langle h_{1I}(\mathbf{x};t) b_{1J}^y(\mathbf{y};0) \rangle_i = \frac{1}{3} \sum_{i < j} X C_{IJ;i_j}(t); \quad (3.35)$$

$$\sum_{x,y} \langle h_I^0(\mathbf{x};t) \frac{G_J^y(\mathbf{y};0)}{J} \rangle_i = C_{IJ;5}(t) \quad 2D_{IJ;5}(t); \quad (3.36)$$

$$\sum_{x,y} \langle h_{!I}(\mathbf{x};t) !_{J}^y(\mathbf{y};0) \rangle_i = \frac{1}{3} \sum_{i=1}^3 [C_{IJ;i}(t) \quad 2D_{IJ;i}(t)]; \quad (3.37)$$

$$\sum_{x,y} \langle h_{f0I}(\mathbf{x};t) f_{0J}^y(\mathbf{y};0) \rangle_i = C_{IJ;1}(t) \quad 2D_{IJ;1}(t); \quad (3.38)$$

$$\sum_{x,y} \langle h_{f1I}(\mathbf{x};t) f_{1J}^y(\mathbf{y};0) \rangle_i = \frac{1}{3} \sum_{i=1}^3 X^3 [C_{IJ;5_i}(t) \quad 2D_{IJ;5_i}(t)]; \quad (3.39)$$

$$\sum_{x,y} \langle h_{h1I}(\mathbf{x};t) h_{1J}^y(\mathbf{y};0) \rangle_i = \frac{1}{3} \sum_{i < j} X C_{IJ;i_j}(t) \quad 2D_{IJ;i_j}(t); \quad (3.40)$$

in terms of the connected and disconnected quark loop contributions (Tr is for over color and spinor indices only),

$$\begin{aligned} C_{IJ}(t) &= \sum_{x,y} \langle \text{Tr} \left[\begin{array}{c} \text{---} \\ q_I(\mathbf{x};t) \text{---} q_I(\mathbf{x};t) q_I(\mathbf{y};0) \text{---} q_I(\mathbf{y};0) \end{array} \right] \rangle \\ &= \sum_{x,y} \text{hTr} [G_{IJ}(\mathbf{x};t;\mathbf{y};0) G_{JI}(\mathbf{y};0;\mathbf{x};t)]_i \quad (= i_5; i_{i1}; i_{5_i}; i_{i_j}); \quad (3.41) \\ D_{IJ}(t) &= \sum_{x,y} \langle \text{Tr} \left[\begin{array}{c} \text{---} \\ q_I(\mathbf{x};t) \text{---} q_I(\mathbf{x};t) q_I(\mathbf{y};0) \text{---} q_I(\mathbf{y};0) \end{array} \right] \rangle \\ &= \sum_{x,y} \langle \text{Tr} [G_{II}(\mathbf{x};t;\mathbf{x};t)] \rangle_X \quad \sum_{x^0} \langle \text{Tr} [G_{II}(\mathbf{x}^0;t;\mathbf{x}^0;t)] \rangle_{iE=9} \\ &\quad + \sum_{x,y} \langle \text{Tr} [G_{JJ}(\mathbf{y};0;\mathbf{y};0)] \rangle_X \quad \sum_{\mathbf{y}^0} \langle \text{Tr} [G_{JJ}(\mathbf{y}^0;0;\mathbf{y}^0;0)] \rangle_{iE=9} \\ &\quad (= i_5; i_{i1}; i_{5_i}; i_{i_j}); \quad (3.42) \end{aligned}$$

Here the $G_{IJ}(\mathbf{x};t;\mathbf{y};t^0)$ is the propagator of the four dimensional quark field

$$G_{LL}^{c_i; \mathbf{x}^0; 0}(\mathbf{x};t;\mathbf{y};t^0) = D^{-1}(\mathbf{x};t;\mathbf{y};t^0) \quad c_i; \mathbf{x}^0; 0; \quad (3.43)$$

$$G_{LS}^{c_i; \mathbf{x}^0; 0}(\mathbf{x};t;\mathbf{y};t^0) = \sum_{c^0} \sum_{\mathbf{x}^0} \langle \text{Tr} [D^{-1}(\mathbf{x};t;\mathbf{x}^0;t^0)] \rangle_{i_c; \mathbf{x}^0; 0} \quad F^{c^0; \mathbf{x}^0}(\mathbf{x}^0;\mathbf{y}); \quad (3.44)$$

$$G_{SL}^{c; c^0; 0}(\mathbf{x}; t; \mathbf{y}; t^0) = \sum_{\mathbf{x}^0} \sum_{\mathbf{y}^0} F^{c; c^0}(\mathbf{x}; \mathbf{x}^0) D^{-1}(\mathbf{x}^0; t; \mathbf{y}; t^0) i_{c^0; c^0; 0}; \quad (3.45)$$

$$G_{SS}^{c; c^0; 0}(\mathbf{x}; t; \mathbf{y}; t^0) = \sum_{\mathbf{x}^0} \sum_{\mathbf{y}^0} F^{c; c^0}(\mathbf{x}; \mathbf{x}^0) D^{-1}(\mathbf{x}^0; t; \mathbf{y}^0; t^0) i_{c^0; c^0; 0} F^{c^0; c^0}(\mathbf{y}^0; \mathbf{y}); \quad (3.46)$$

where D^{-1} is written in terms of inverse of the five dimensional matrix D_{DWF}^{-1} (eq. (3.2)):

$$\begin{aligned} D^{-1}(\mathbf{x}; \mathbf{y}) &= \sum_{\mathbf{s}} \sum_{\mathbf{s}^0} q(\mathbf{x}) q(\mathbf{y}) \\ &= \sum_{\mathbf{s}; \mathbf{s}^0} \frac{1}{2} \left(\frac{1 + \gamma_5}{2} \right)_{\mathbf{s}; \mathbf{s}^0} D(\mathbf{x}; \mathbf{s}) E(\mathbf{y}; \mathbf{s}^0) \left(\frac{1 + \gamma_5}{2} \right)_{\mathbf{s}; \mathbf{s}^0} + \frac{1}{2} \left(\frac{1 - \gamma_5}{2} \right)_{\mathbf{s}; \mathbf{s}^0} \\ &= \sum_{\mathbf{s}; \mathbf{s}^0} \frac{1}{2} \left(\frac{1 + \gamma_5}{2} \right)_{\mathbf{s}; \mathbf{s}^0} D_{DWF}^{-1}(\mathbf{x}; \mathbf{s}; \mathbf{y}; \mathbf{s}^0) \left(\frac{1 + \gamma_5}{2} \right)_{\mathbf{s}; \mathbf{s}^0} + \frac{1}{2} \left(\frac{1 - \gamma_5}{2} \right)_{\mathbf{s}; \mathbf{s}^0} \end{aligned} \quad (3.47)$$

$F(\mathbf{x}; \mathbf{y})$ is smearing function which is defined in eq.(3.14).

$c; c^0; c^m; c^m$ are color index and $; 0$ are spin index. We apply the zero momentum projection for quark operators to obtain the meson mass from meson energy, $E_p = \sqrt{m_{meson}^2 + \mathbf{p}^2}$, by sum over spatial volume $\mathbf{x}; \mathbf{x}^0; \mathbf{y}; \mathbf{y}^0$. In equation (3.41), the sum over \mathbf{y} is stochastically evaluated by using the Z_2 noise source at $t = 0$, while the sums over \mathbf{x} and \mathbf{y} in (3.42) are done by Z_2 source spreads over space-time volume, c.f. (3.19) and (3.20):

$$\begin{aligned} & \frac{1}{N_{noise}} \sum_{n=1}^{N_{noise}} \sum_{\mathbf{x}; \mathbf{y}; \mathbf{z}} \text{hTr} [f G_{IJ}(\mathbf{x}; t; \mathbf{y}; 0)^{(n)} (\mathbf{y}; 0) g_{5IJ}(\mathbf{x}; t; \mathbf{z}; 0)^{(n)} (\mathbf{z}; 0) g_{5IJ}^{-1}(\mathbf{z}; 0) g_{5IJ}^{-1}(\mathbf{x}; t; \mathbf{y}; 0)] \\ &= \frac{1}{N_{noise}} \sum_{n=1}^{N_{noise}} \sum_{\mathbf{x}; \mathbf{y}; \mathbf{z}} \text{hTr} [G_{IJ}(\mathbf{x}; t; \mathbf{y}; 0) G_{IJ}^Y(\mathbf{x}; t; \mathbf{z}; 0) g_{5IJ}^{-1}(\mathbf{z}; 0) g_{5IJ}^{-1}(\mathbf{x}; t; \mathbf{y}; 0)] \\ & \quad \times \text{hTr} [G_{IJ}(\mathbf{x}; t; \mathbf{y}; 0) G_{IJ}^Y(\mathbf{x}; t; \mathbf{y}; 0) g_{5IJ}^{-1}(\mathbf{x}; t; \mathbf{y}; 0) g_{5IJ}^{-1}(\mathbf{x}; t; \mathbf{y}; 0)] (N_{noise} - 1); \\ &= \sum_{\mathbf{x}; \mathbf{y}} \text{hTr} [G_{IJ}(\mathbf{x}; t; \mathbf{y}; 0) G_{JI}(\mathbf{y}; 0; \mathbf{x}; t)] \quad (3.48) \end{aligned}$$

$$\begin{aligned} & \frac{1}{N_{noise}} \sum_{n=1}^{N_{noise}} \sum_{\mathbf{x}; \mathbf{y}; t^0} \text{hTr} [f^{(n)}(\mathbf{x}; t) f G_{II}(\mathbf{x}; t; \mathbf{y}; t^0)^{(n)} (\mathbf{y}; t^0) g_{II}(\mathbf{y}; t^0)] \\ & \quad \times \text{hTr} [G_{II}(\mathbf{x}; t; \mathbf{x}; t)] \quad (N_{noise} - 1); \quad (3.49) \end{aligned}$$

The dagger is taken only for color and spinor (not for the space-time) indices, and we use the γ_5 hermiticity, $\gamma_5 D^{-1} \gamma_5 = \mathbb{D}^{-1} \gamma_5$, of the propagator (3.47) in the last equation in (3.48). The trace over color and spinor is done exactly by solving the quark propagator 3-4 times each for a random source.

3.5. Meson Mass Fit

Throughout this paper, we assume the one particle state is the ground state for each quantum numbers, $I; J^{PC}$, compatible to the interpolation operator in Table II. This assumption is not entirely true for some cases in real nature. For example, meson could decay into pions. In our simulation, quarks are still kept heavy, the lightest quark mass is about half of strange quark mass, confined in the relatively small $(2 \text{ fm})^3$ box. So many of the decaying processes would not happen in this setting since the decaying particles have energy above the threshold. Also we restrict ourselves to degenerate up and down quarks, $N_f = 2$, so some meson such as a_0 can't decay due to exact symmetries.

To extract the meson masses, the following two analyses are carried out.

(A) Standard method:

Only the ground state of mass m_0 is assumed to exist in the correlation function $\langle O_S O_S^\dagger \rangle$, which is fitted by the hyperbolic cosine function reflecting the periodic boundary condition for meson at $t = T$,

$$\sum_{x,y} \langle O_I(\mathbf{x};t) O_I^\dagger(\mathbf{y};0) \rangle = \frac{V}{2m_0} \langle \mathcal{D}_I \mathcal{D}_I^\dagger(\mathbf{p}=\mathbf{0}) \rangle^2 e^{-m_0 t} + e^{-m_0 (T-t)}; \quad (I = L; S) \quad (3-50)$$

for large enough t and $T-t$. Although our main results will be obtained from smeared quarks case, $I = S$, we also analyze on local quarks to monitor the excited state contamination. The fitting range of t is determined so that the effective meson mass becomes independent of the timeslice. We also avoid too large t where the statistical error become large and unreliable.

(B) Variational method:^{(27),(28)}

In this case, we also assume the first excited state of mass m_0 . Both the local ($I; J = L$) and the smeared ($I; J = S$) interpolation fields are used to construct $\langle O_I O_J^\dagger \rangle$ correlation function. The 2×2 matrix,

$$X(t) = \begin{pmatrix} \sum_{x,y} \langle O_L(\mathbf{x};t) O_L^\dagger(\mathbf{y};0) \rangle & \sum_{x,y} \langle O_L(\mathbf{x};t) O_S^\dagger(\mathbf{y};0) \rangle \\ \sum_{x,y} \langle O_S(\mathbf{x};t) O_L^\dagger(\mathbf{y};0) \rangle & \sum_{x,y} \langle O_S(\mathbf{x};t) O_S^\dagger(\mathbf{y};0) \rangle \end{pmatrix}; \quad (3-51)$$

is normalized at a reference timeslice t_0 to reduce the statistical error, then diagonalized as

$$X^{-1/2}(t_0) X(t) X^{-1/2}(t_0) \stackrel{\text{diag.}}{=} \begin{pmatrix} \langle O_L(t; t_0) O_L^\dagger(t_0) \rangle & 0 \\ 0 & \langle O_S(t; t_0) O_S^\dagger(t_0) \rangle \end{pmatrix}; \quad (3-52)$$

The eigenvalues are fit as a function of t ,

$$\langle O_I(t; t_0) O_I^\dagger(t_0) \rangle = \frac{e^{-m_0 t} + e^{-m_0 (T-t)}}{e^{-m_0 t_0} + e^{-m_0 (T-t_0)}} e^{-m_0 (t-t_0)}; \quad (3-53)$$

$$a_0(t; t_0) = \frac{e^{-m_0 t} + e^{-m_0 (T-t)}}{e^{-m_0 t_0} + e^{-m_0 (T-t_0)}} e^{-m_0 (t-t_0)}; \quad (3.54)$$

to obtain the masses of the states.

The second method, called variational method, is employed to extract the ground state energy precisely and to check the amount of excited state contamination.

To fit $a_0(t; t_0)$ as Eq. (3.53), without unknown amplitudes in front of the exponentials, t_0 should be enough large to ignore the higher excited states. By monitoring $a_0(t; t_0)$, we check, for our choice of t_0 , such contamination is not visible within current statistics. For example, $t_0 = 2$ (box) is our choice in Fig. 2. $a_0(t; t_0)$ for $t_0 = 1$ (circle) is not a single exponential, while those of $t_0 > 2$ (diamond, triangle) have larger error bars. If the number of available configurations were larger, we would have seen the effect from the second excited state, and should have calculated from more variation of interpolation field. This point could be important for future investigations with higher statistics.

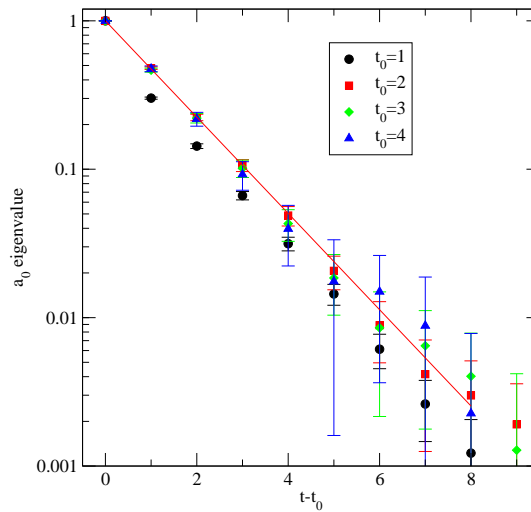


Fig. 2. t_0 dependence of a_0 eigenvalue for $m_f = 0.02$. We chose $t_0 = 2$ (box) by checking the higher excited states contamination.

As an example, a_0 effective masses, which we will define in (4.1), from the two methods are plotted in Fig. 3. The effective mass from the variational method (box) has the smallest statistical error, which is consistent with that of standard method using smeared-smeared interpolation field (filled circle). For the variational method, the plateau starts from smaller time distance as the excited state is separated from the ground state. Their global fits to the plateaux are almost identical to each other. The clear signal of larger excited state

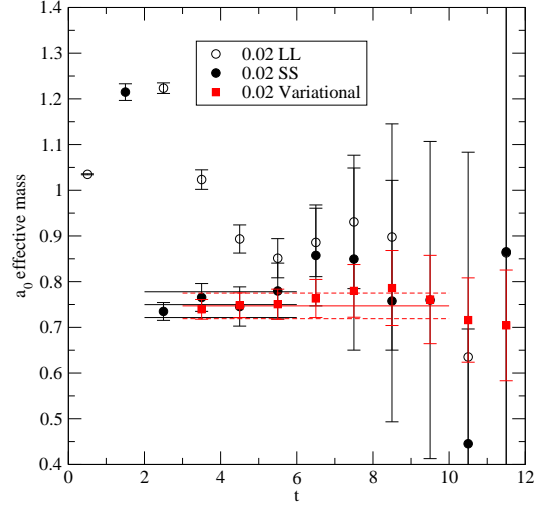


Fig. 3. Comparison of the a_0 effective mass obtained by the two methods. Circle empty (filled) symbol show the results from the local-local (smeared-smeared) interpolation field in the standard method while box is the effective mass obtained in the variational method.

contamination for local-local interpolation field (empty circle) is seen. The identical central values and error bars from the standard single exponential fit and the variational method indicate the effect from excited states is small for both of methods with these settings.

We analyze both methods for all masses and compare to estimate systematic uncertainty from higher excited states. We will also explore the first excited state for pseudoscalar and vector meson, π , ρ , ω , using the variational methods.

3.6. Decay Constant

The leptonic decay constant could be obtained from the amplitude of the two point correlation function of meson. We analyze decay constants for pion, ρ and ω mesons. Their decay constants, f_π , f_ρ and f_ω could be defined through the conserved axial and vector currents, $A^b(x)$ and $V_i^b(x)$,

$$f_{\pi^0} m_\pi = \langle 0 | \mathcal{A}_4^b(x) | \rho(\mathbf{p} = \mathbf{0}) \rangle = Z_A \langle 0 | \mathcal{A}_4^b(x) | \rho(\mathbf{p} = \mathbf{0}) \rangle \quad (0 = \pi^0; \rho^0); \quad (3-55)$$

$$f_{\rho^i} m_\rho = \langle 0 | \mathcal{V}_i^b(x) | \rho(\mathbf{p} = \mathbf{0}) \rangle = Z_V \langle 0 | \mathcal{V}_i^b(x) | \rho(\mathbf{p} = \mathbf{0}) \rangle \quad (i = 1; 2; 3); \quad (3-56)$$

where \mathbf{e}_i is the polarization vector of the vector meson state, and Z_A, Z_V are the matching factors between the lattice local currents

$$A^b(x) = q(x) \gamma_5 \gamma^b q(x); \quad (3-57)$$

$$V^b(x) = q(x)^b q(x): \quad (3-58)$$

$$(3-59)$$

and an appropriate renormalization scheme in the continuum QCD, which, in our case, is \overline{MS} at $\mu = 2 \text{ GeV}$.

For f and f' , the first matrix element in (3-55) could be related to that of pseudoscalar density $P^b(x;t) = q(x)^b q(x)$ using (flavor non-singlet) AWTL,

$$\langle 0 | \mathcal{P}^b(x) | 0 \rangle = 2(m_f + m_{res}) \langle 0 | \mathcal{P}^b(x) | 0 \rangle \quad (3-60)$$

and leads to

$$f_0 m_0^2 = 2(m_f + m_{res}) \langle 0 | \mathcal{P}^b | 0 \rangle \quad (3-61)$$

The actual determination for the decay constants is done by the standard method, (C), for pion and meson, and the variational method, (D), for pion and η' :

(C) Standard method

In this case we assume the $\langle h_L | h_L \rangle$ and $\langle h_L | h_L \rangle$ correlation functions contains only the ground state propagation. $\langle h_L | h_L \rangle$ and $\langle h_L | h_L \rangle$ are fitted by a standard hyperbolic cosine function,

$$\begin{aligned} \langle h_L(x;t) | h_L(y;0) \rangle &= \frac{V}{2m} \langle 0 | \mathcal{P}_L^a | 0 \rangle^2 e^{-m|t|} + e^{-m(\tau-t)} \\ &= \frac{V f^2 m^3}{8(m_f + m_{res})^2} e^{-m|t|} + e^{-m(\tau-t)}; \end{aligned} \quad (3-62)$$

$$\begin{aligned} \langle h_L(x;t) | h_L(y;0) \rangle &= \frac{V}{2m} \langle 0 | \mathcal{Y}_L^a | 0 \rangle^2 e^{-m|t|} + e^{-m(\tau-t)} \\ &= \frac{V f^2 m}{2Z_V^2} e^{-m|t|} + e^{-m(\tau-t)}; \end{aligned} \quad (3-63)$$

to extract the quantities m , f , m , and $f = Z_V$.

(D) Variational method

In this case, the second excited state, η' , in the correlation function of the local meson operator, $\langle h_L | h_L \rangle$, is also taken into account. $\langle h_L | h_L \rangle$ is fitted by a double hyperbolic cosine function:

$$\begin{aligned} \langle h_L(x;t) | h_L(y;0) \rangle &= \frac{V}{2m} \langle 0 | \mathcal{P}_L^a | 0 \rangle^2 e^{-m|t|} + e^{-m(\tau-t)} \\ &\quad + \frac{V}{2m} \langle 0 | \mathcal{P}_L^a | 0 \rangle^2 e^{-m|t|} + e^{-m(\tau-t)} \\ &= \frac{V f^2 m^3}{8(m_f + m_{res})^2} e^{-m|t|} + e^{-m(\tau-t)} + \frac{V f^2 m^3}{8(m_f + m_{res})^2} e^{-m|t|} + e^{-m(\tau-t)} \end{aligned} \quad (3-64)$$

In this procedure, we first determine m and m by the variational method, method (B) in previous subsection, and then fit the two point function data to (3.64) to determine the two quantities, f ; f using the results from the first fit under the jackknife.

3.7. Chiral Extrapolation

To obtain masses and decay constants of various mesons at the physical quark mass point, $m_f = m_{\text{u,d}}$ ²⁴⁾ we need to extrapolate the numerical value calculated at heavier quark mass points. As the number of the simulation points are limited, and the statistical error is too large, we do not use the formula of the chiral perturbation theory at the next leading order or higher in this work.

As a crude estimation of the 0 mass at the physical point, we examine the formula valid in the lowest order approximation from the flavor singlet axial Ward-Takahashi identity Eq. (3.60)

$$m^2_0 = C_0 + C_1 (m_f + m_{\text{res}}) \quad (\text{AWTI type}); \quad (3.65)$$

We also try the simplest linear extrapolation for all meson masses as well as the decay constants,

$$O = C_0 + C_1 (m_f + m_{\text{res}}) \quad (\text{linear type}); \quad (3.66)$$

where O is either a meson mass or a decay constant.

4. Numerical Results

4.1. mass and lattice scale

First we analyze meson mass using the two methods and determine the lattice scale from m assuming it is a stable particle which is true for the relatively heavy quark in the small box used in our simulation. In Figure 4, meson's effective mass, taken from the damping rate between meson propagators at two neighboring time slices, $m^e_{;IJ}(t+1=2)$, which is defined as

$$\frac{\begin{matrix} P & D & E \\ \begin{matrix} x_{xy} \\ \begin{matrix} O_I(x;t)O_J^y(y;0) \\ \begin{matrix} O_I(x;t+1)O_J^y(y;0) \end{matrix} \end{matrix} \end{matrix} \end{matrix}}{E} = \frac{e^{-m^e_{;IJ}(t+\frac{1}{2})t} + e^{-m^e_{;IJ}(t+\frac{1}{2})(T-t)}}{e^{-m^e_{;IJ}(t+\frac{1}{2})(t+1)} + e^{-m^e_{;IJ}(t+\frac{1}{2})(T-t-1)}} \quad (4.1)$$

is plotted in the top panels (using method (A) on the left and method (B) on the right panels). On the bottom panel, we show an eigenvalue of the ground state from the variational method. The results of m are listed in Table 4.1 from the standard hyperbolic cosine fit (method (A)) and the variational method (method (B)). The masses from both methods are

consistent to each other within statistical error for all m_f , and the ground state mass would be extracted successfully by the smeared operator.

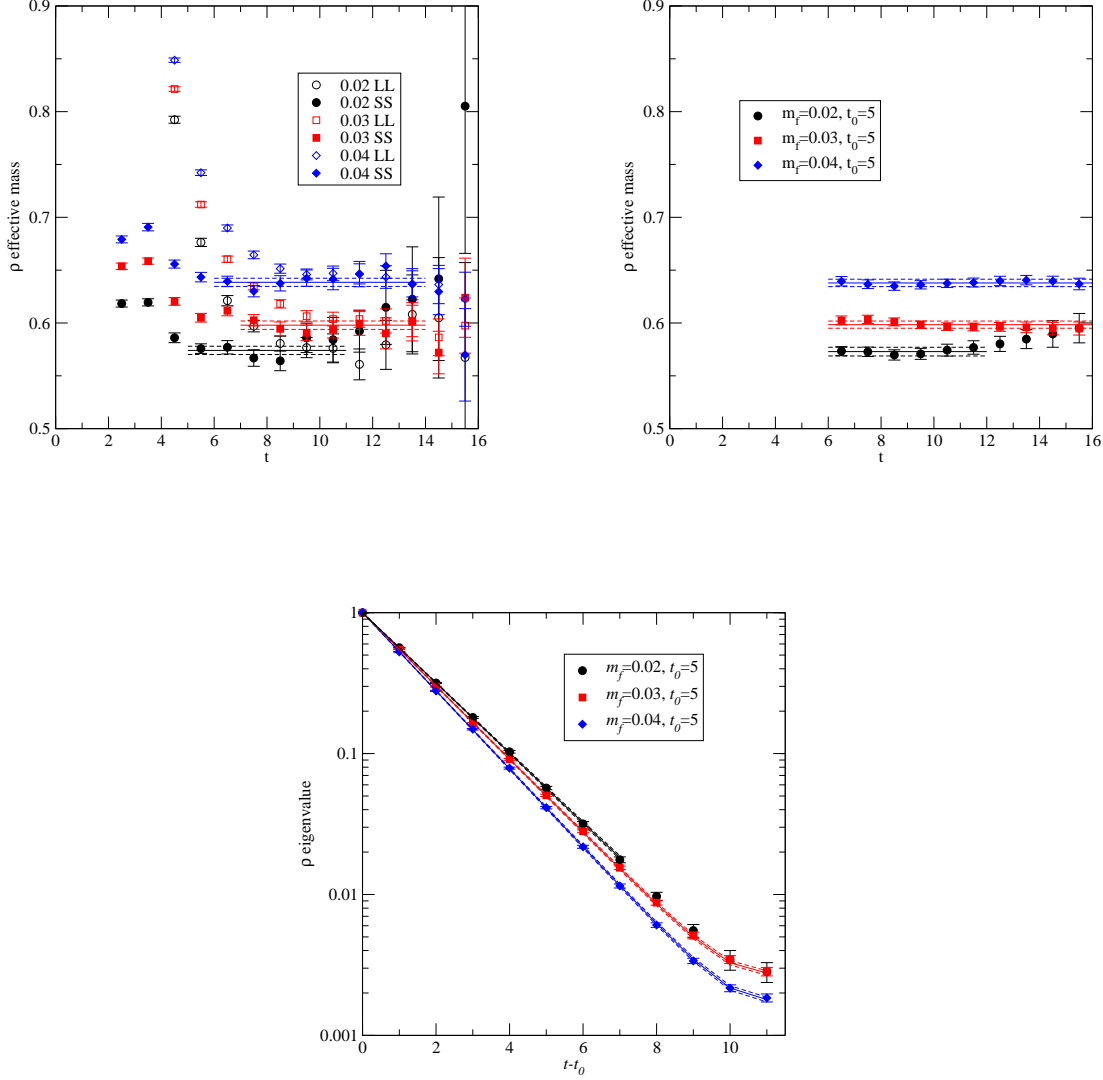


Fig. 4. Effective mass vs. t using method (A) (left) and method (B) (right), and eigenvalue vs. $t - t_0$ (bottom). Lines show the global fit result, with errors and ranges of fit.

We perform linear extrapolation for both results and obtain m at physical quark mass point ($m_f = m_{u,d}$). The result of the chiral extrapolation is shown in Figure 5 and Table IV. The values from both methods at physical quark mass point are consistent within statistical error, we choose the value from method (B) as our main value. A lattice scale determined

Table III. m

m_f	m	t_0	$t_{m \text{ in}}$	$t_{m \text{ ax}}$	method
0.02	0.5741 (39)		5	11	(A)
	0.5729 (41)	5	$t_0 + 1$	12	(B)
	0.5425 (64) ^a		5	16	(A)
0.03	0.5979 (40)		7	14	(A)
	0.5984 (34)	5	$t_0 + 1$	16	(B)
	0.5946 (58) ^a		6	16	(A)
0.04	0.6385 (39)		6	14	(A)
	0.6379 (35)	5	$t_0 + 1$	16	(B)
	0.6323 (70) ^a		7	16	(A)

(a) These values are obtained from $(I;J) = (L;W)$ correlation functions and quoted by²⁴⁾

from $m = 775.49 \text{ MeV}^{-1}$ is

$$a_m^{-1} = 1.537 (26) \text{ GeV} \quad (4.2)$$

We have measured the potential energy between static quarks and extract Sommer scale, r_0 from the potential $r_0 = a = 4.278 (54)$.²⁴⁾ Using a_m we find

$$r_0^{\text{phys}} = 0.5491 (93) \text{ fm} \quad (4.3)$$

which is somewhat larger length than previously estimated values by 10%. Although r_0 is one of the most precisely determined dimensional quantities in lattice QCD, its experimental value is not known, we couldn't judge whether our larger value is closer to the physical value in QCD or it reflects some systematic errors that we discuss in later section.

By increasing the statistics, lattice scale changed from the one we reported in the previous paper.²⁴⁾ Accordingly, the physical quark mass point, $m_f = m_{\text{u,d}}$, could change. However we use the old value of $m_{\text{u,d}}$ as the physical quark mass point in this paper. This is because the number of quark mass points newly obtained in this work is not sufficient to repeat the same analysis as before in which we went to the next to the leading order ChPT. We will discuss decay constant and excited state meson, ρ , later sections.

4.2. pion mass

In Figure 6, we plot the effective mass of pseudoscalar meson by method (A) on the left, method (B) on the right panel, and the ground state eigenvalue using method (B) on the bottom panel. Table V summarizes the values of pion mass t obtained by both methods. By increasing 5-10 times larger statistics than previous analysis, and extracting the ground

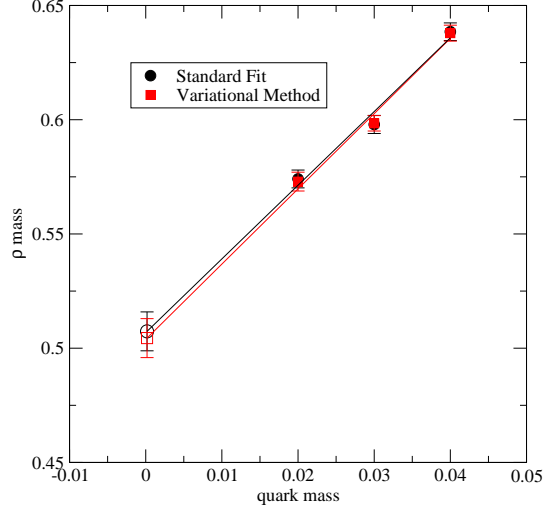


Fig. 5. m_ρ vs. m_f

Table IV. m_ρ at the physical quark mass point ($m_f = m_{u,d}$)

m	a_m^{-1} [GeV]	a_m [fm]	m method
0.5073 (85)	1.528 (26)	0.1291 (22)	(A)
0.5044 (85)	1.537 (26)	0.1284 (22)	(B)

state information from meson propagator at shorter time distance, which becomes possible by using smeared operators, the statistical errors decrease approximately by half of previous results. The fact that the reduction of the error size is closer or even larger than that expected from the increase of the number of statistical sample, $1/2 > 1/\sqrt{5-10}$, suggests that the smearing itself is not necessarily cause the smaller statistical error for pseudoscalar meson. Rather we could check the information of the excited state contamination by having the smeared operators which has the different overlaps to the states. In fact, our new results are consistent within statistical error to the previous results. We will discuss decay constant and excited state meson, , later.

4.3. a_0 mass

From experiments, there are two flavor-non-singlet scalar mesons, $a_0(980)$ and $a_0(1450)$, in nature. Although these are unstable particles in more realistic $N_f = 2+1$ case, we assume a stable one particle state to be the ground state in the scalar meson sector in our $N_f = 2$ with relatively heavy quark and small space-time. Previous a_0 meson spectrum results in

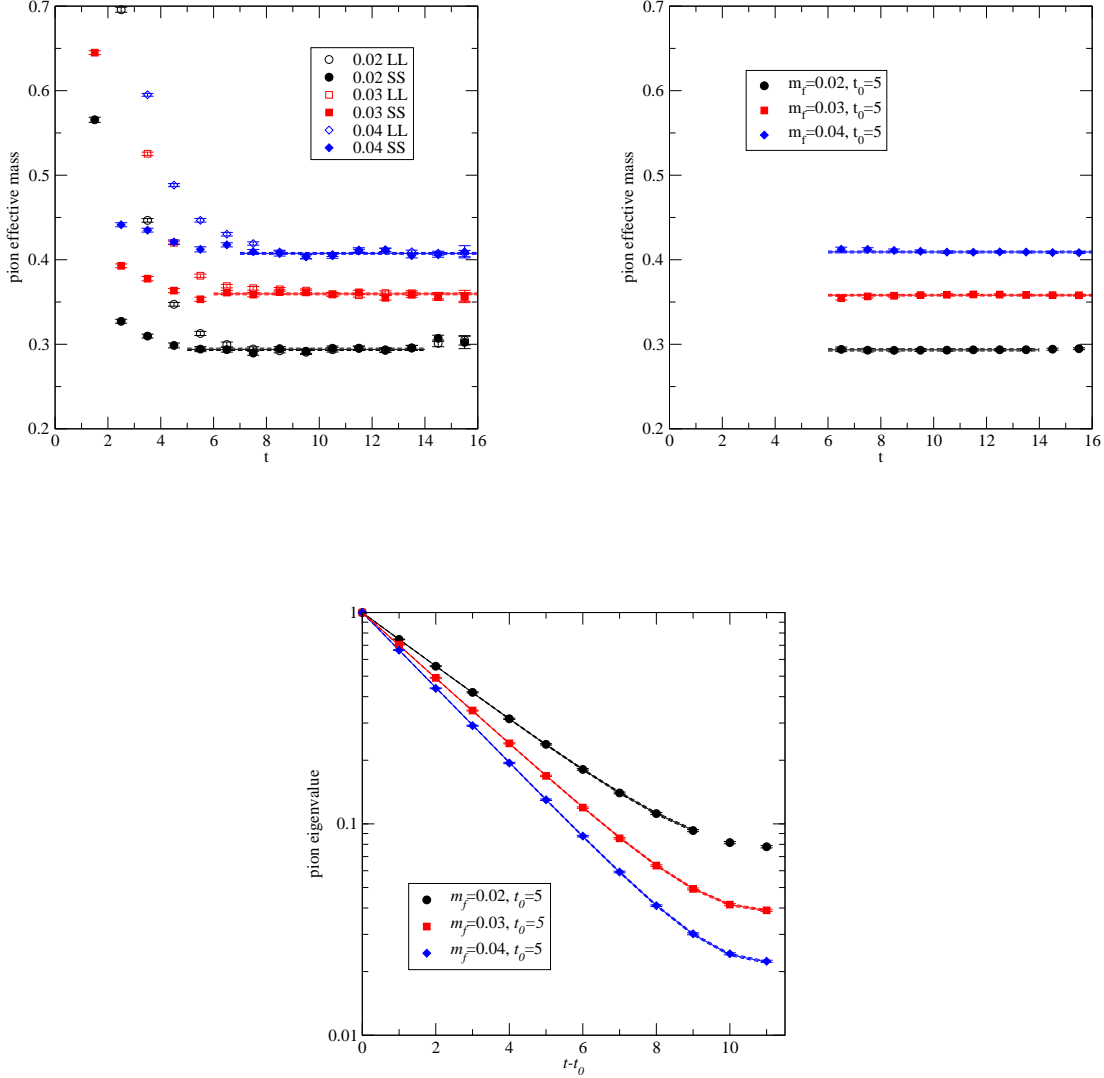


Fig. 6. Pion effective mass vs. t using method (A) (left) and method (B) (right), and pion eigenvalue vs. $t - t_0$ (bottom). Lines show fit values, errors and ranges.

lattice QCD calculation seems to scatter⁴²⁾ roughly into two categories, the ones report lighter masses ~ 1 GeV^{41),43)} and the others support heavier masses ~ 1.5 GeV.^{25),42),44),45)} Previous RBC's results²⁵⁾ are $m_{a_0} = 1.58(34)$ GeV in analysis for unitary points and 1.51 (19) GeV in the partially quenched analysis.

Figure 7 (left) shows a_0 effective mass, Figure 7 (right) shows eigenvalue of the ground state using variational method (B). The numerical values are listed in Table VI, in which we also quote RBC's previous values.²⁵⁾

Table V. m

m_f	m	t_0	$t_{m \text{ in}}$	$t_{m \text{ ax}}$	method
0.02	0.2940 (14)		5	14	(A)
	0.2934 (13)	5	$t_0 + 1$	14	(B)
	0.2902 (28) ^a		9	16	(A)
0.03	0.3596 (11)		6	16	(A)
	0.3581 (10)	5	$t_0 + 1$	16	(B)
	0.3575 (19) ^a		9	16	(A)
0.04	0.4075 (11)		7	16	(A)
	0.4092 (11)	5	$t_0 + 1$	16	(B)
	0.4094 (25) ^a		9	16	(A)

(a) These values are obtained from $(I;J) = (L;W)$ correlators and quoted by²⁴⁾

Our new results for $a_0 m$ mass is significantly lighter than that of previous results as seen in the Table VI. Since the QCD ensemble used in both investigation are same, this discrepancy must come from the difference in measuring meson operator. In previous calculation the meson interpolation field was constructed from quark fields at a point. Although the point operator was convenient for theoretical investigation in previous study, it is not necessary optimal for extracting the ground state. In fact, as seen in the left panel of Figure 7, the effective mass of point operator (empty symbols) is very large at short distance, which implies rather large excited state contamination in the point operator. On the other hand, the mass using the smeared operator in this figure (filled symbols) has better plateaux from shorter distance and coincide to that from the ground state eigenvalue of the variational method shown in right panel. We also note that the number of statistical sample is increased by a factor of five or more for this work compared to that in the previous report.

Figure 8 shows results of extrapolation by linear fit and Table VII shows m_{a_0} at the physical quark mass point. Since both methods (A) and (B) are consistent to each other we choose m_{a_0}

$$m_{a_0}^{\text{phys}} = 1.111 (81) \text{ GeV} \quad (4.4)$$

from method (B) as our final value in this work.

To settle down the discrepancies among lattice calculations and that from experiments, further investigations including calculation for the multi particle scattering states and the strange sea quark effects ($N_f = 2 + 1$) are needed.

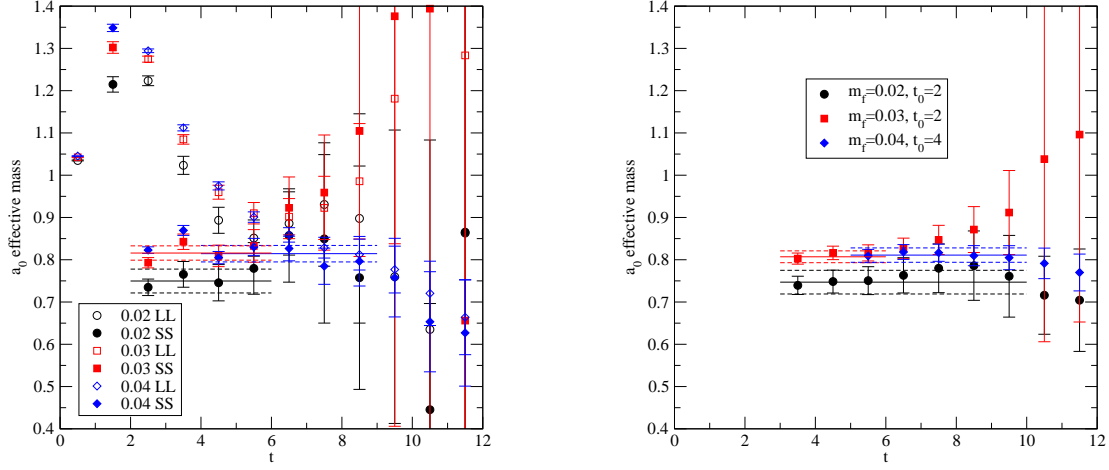


Fig. 7. a_0 effective mass vs. t using method (A) (left) and method (B) (right). Lines show t values, errors and ranges.

Table VI. m_{a_0}

m_f	m_{a_0}	t_0	$t_{m \text{ in}}$	$t_{m \text{ ax}}$	method
0.02	0.750 (28) ^a		2	6	(A)
	0.747 (28)	2	$t_0 + 1$	10	(B)
	0.92 (9) ^b		4	10	exponential t
0.03	0.816 (17) ^a		2	6	(A)
	0.807 (14)	2	$t_0 + 1$	6	(B)
	0.99 (10) ^b		5	10	exponential t
0.04	0.814 (19) ^a		4	9	(A)
	0.811 (17)	4	$t_0 + 1$	10	(B)
	0.94 (5) ^b		5	12	exponential t

(a) These values are obtained by uncorrelated t . (b) These values are obtained from $(I;J) = (L;L)$ correlators and quoted by.²⁵⁾

4.4. 0 mass

Before presenting the mass spectrum results of the flavor singlet pseudoscalar meson, 0 , we check whether the theoretical expectation discussed in Section 2 is realized. The ratio of the correlation function between disconnected quark loops, $D_s(t)$, to the connected correlator, $C_s(t)$, was discussed to approach to unity in large time separation, which is clearly different from the expectation of the linear growth in the quenched QCD case (2.8).

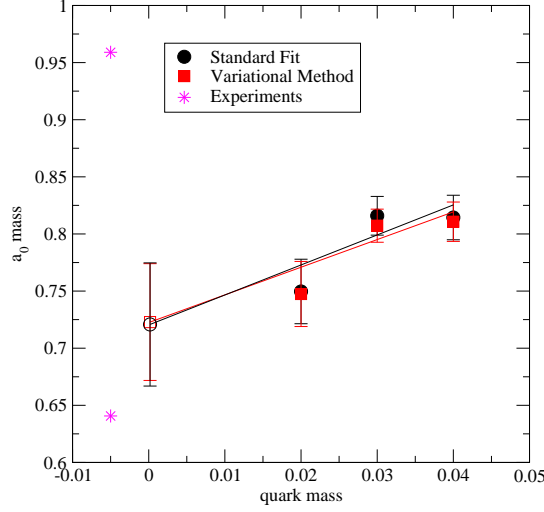


Fig. 8. m_{a_0} vs. m_f . The left most star symbol shows the experimental values¹⁾ in the real world.

Table V II. m_{a_0} at the physical quark mass point ($m_f = m_{u,d}$)

m_{a_0}	$m_{a_0}^{\text{phys}}$ [MeV]	$m_{a_0} r_0$	method
0.721 (54)	1,108 (85)	3.08 (23)	(A)
0.723 (51)	1,111 (81)	3.10 (22)	(B)

In the discussion, only pion and 0 state were considered to couple to the $I(J^P) = 0(0^-)$ operator, leading

$$\frac{N_f D_5(t)}{C_5(t)} = 1 - B \frac{e^{-m_0 t} + e^{-m_0(\tau-t)}}{e^{-m_1 t} + e^{-m_1(\tau-t)}} \neq 1 - B e^{-(m_0 - m_1)t}; \quad (4.5)$$

In Figure 9, the ratio extracted using smeared operator, $\frac{0}{s}$, are plotted. Indeed the ratio asymptotically approach to one for lighter two quark masses (circle, box), though they are statistically uncertain at large time distance. However the heaviest quark mass point (diamond) seem s to approach to lower value than one. The mass difference between 0 and $^+$ becomes smaller for heavier quark mass, and is close to zero at the heaviest quark mass (as we will see below), so the approaching to unity only happens at very large t from (4.5). Moreover, this deviation from the simplest theoretical explanation might be due to the omission of the excited states such as $^+$ or 0^+ glueball state, which may play more significant role in the heavier quark mass region. Within the current statistics, we can't conclude if the deviation from the unity on the heaviest quark could be explained by the above mentioned arguments

or other reasons, for example, insufficient sampling of the different topological sectors.

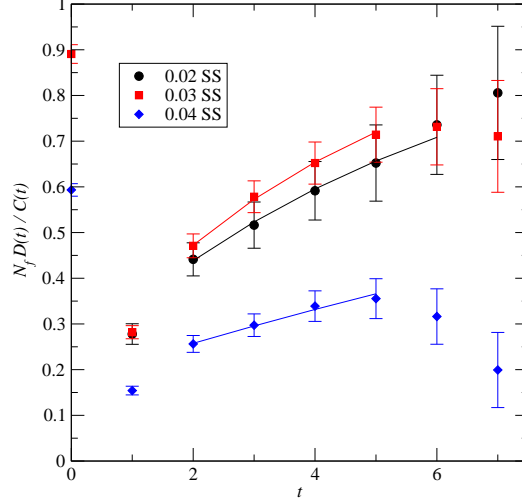


Fig. 9. $N_f D_5(t) = C_5(t)$ vs. t .

We now describe about the ρ spectrum results using method (A) and (B). Figure 10 shows effective mass (left: method (A) and right: method (B)), and the ground state eigenvalue, and their numerical values and their t ranges are in Table V III. We didn't use propagator from longer distance, where the statistics is too poor and the standard error analysis would not be reliable, though including one or two more time slices does not change the t results for most of the masses. The method (B) turns out to have better plateaux than that from method (A) for this meson.

As a consistency check, we also examine the temporal exponent of the ratio (2.6) to extract ρ mass. The t results turn out to be insensitive whether we fit to the second function form or the third formula of (2.6). Combining with the measured pion mass in Table V, $m_\rho = 0.458(58); 0.571(48), 0.461(15)$ for $m_f = 0.02, 0.03, 0.04$. These estimations are slightly smaller than results in Table V III. We have checked the effect of finiteness of lattice in the temporal direction by fitting the second formula in (2.6), and found the results unchanged. One reason could be the time range used in fitting the ratio is too short and pion mass is overestimated, which cause the estimation for ρ mass smaller than reality. Based on this doubt, we will not use the results from the ratio fit in our main results.

ρ mass has only small dependence to the quark mass as seen in Figure 11, all three masses are consistent within two to three sigmas of statistical error, Their central value fluctuates

non monotonically in quark mass order. Before taking this non-monotonicity seriously, we should suspect unreliability of the error estimation and other systematic uncertainties such as insufficient sampling over the topological charge since η^0 likely depends on topological charge strongly. In our simulation we use DBW2 gauge action to reduce the size of the residual chiral symmetry breaking, m_{res} , sacrificing configuration's mobility among different topological sectors to some extent.

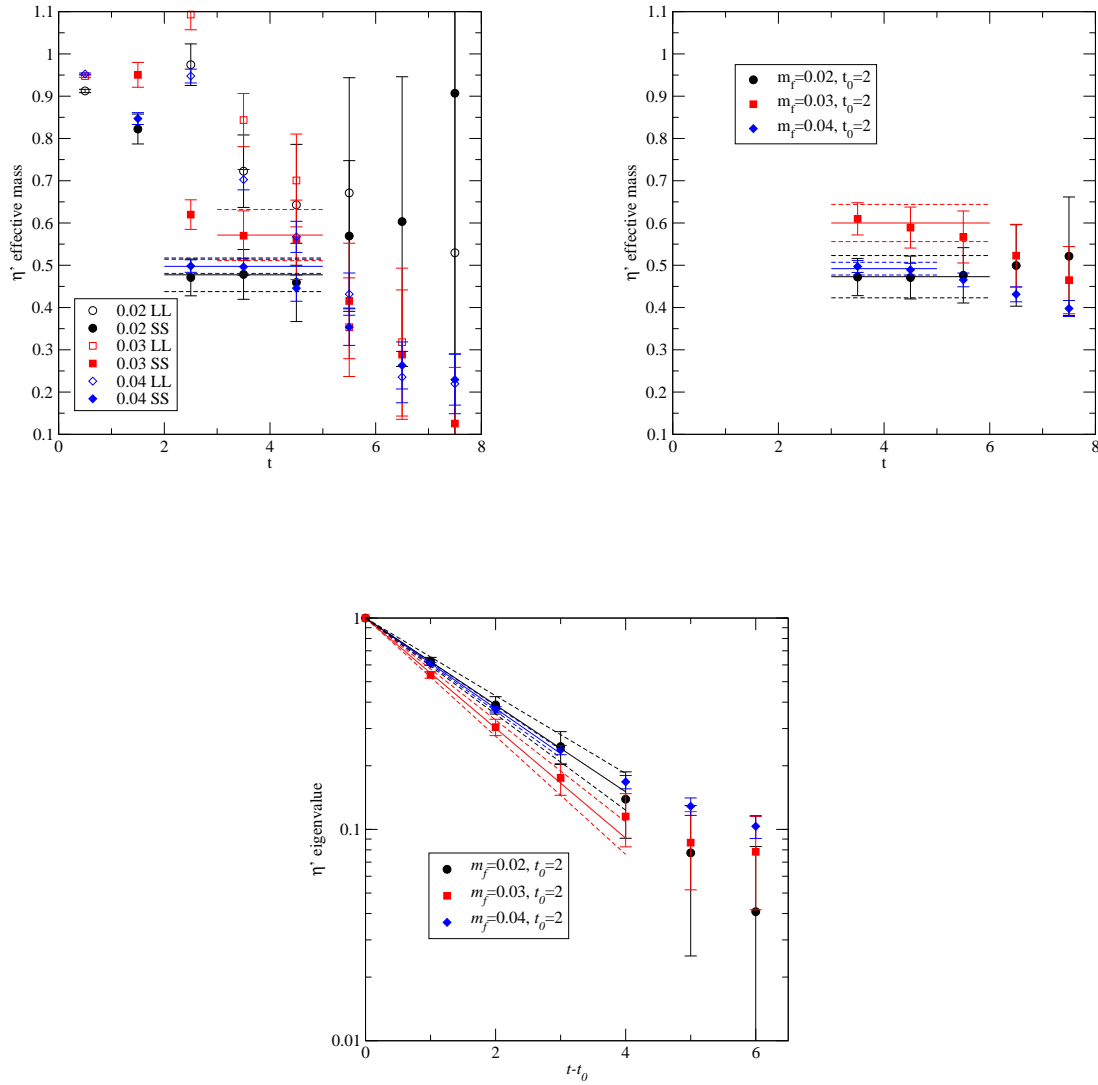


Fig. 10. η^0 effective mass vs. t using method (A) (left) and method (B) (right), and η^0 eigenvalue vs. $t - t_0$ (bottom).

Although quark mass dependence would not be resolved clearly enough, we extrapolate

Table VIII. m_0

m_f	m_0	t_0	t_{min}	t_{max}	method
0.02	0.477 (40)		2	5	(A)
	0.473 (50)	2	$t_0 + 1$	6	(B)
0.03	0.571 (60)		3	5	(A)
	0.600 (44)	2	$t_0 + 1$	6	(B)
0.04	0.497 (17)		2	5	(A)
	0.492 (15)	2	$t_0 + 1$	5	(B)

the measured masses by the two formula (3.65) and (3.66) to estimate 0 mass at the physical quark mass point. The results are shown in Figure 11 and Table IX. The central value of the estimation differ by 15% to each other but within statistical error. Our main estimation for 0 mass at the physical quark mass point is from the variational method (B) and chiral extrapolation using the lowest order of ChPT (3.65),

$$m_0^{phys} = 819(127) \text{ MeV} \quad (4.6)$$

This is the first estimation of 0 mass performed with two flavors of dynamical (approximately) chiral fermion, which is certainly heavier than pion which would be related to the chiral $U(1)_A$ anomaly. Besides the large statistical error and the various systematic error discussed above, the main result is close to the experimental 0 mass, which encourages further improvements especially calculation on $N_f = 2 + 1$ ensemble.

Table IX. m_0 at the physical quark mass point ($m_f = m_{ud}$)

m_0	m_0^{phys} [MeV]	$m_0 r_0$	method and chiral extrapolation
0.480 (78)	738 (121)	2.05 (33)	(A) AW TI type (3.65)
0.487 (78)	748 (120)	2.08 (33)	(A) linear type (3.66)
0.532 (82)	819 (127)	2.28 (35)	(B) AW TI type (3.65)
0.560 (89)	862 (130)	2.40 (36)	(B) linear type (3.66)

4.5. ρ mass

We also examine flavor singlet vector meson, ρ , using the similar procedure as 0 . Figure 12 shows ρ 's effective mass (left: method (A), right: method (B)), which are also listed in Table X. We are able to extract non-zero signal, but, from shorter time distance, so there may be a significant distortion from the excited states. Results on the lightest $m_f = 0.02$ point has especially poor signal.

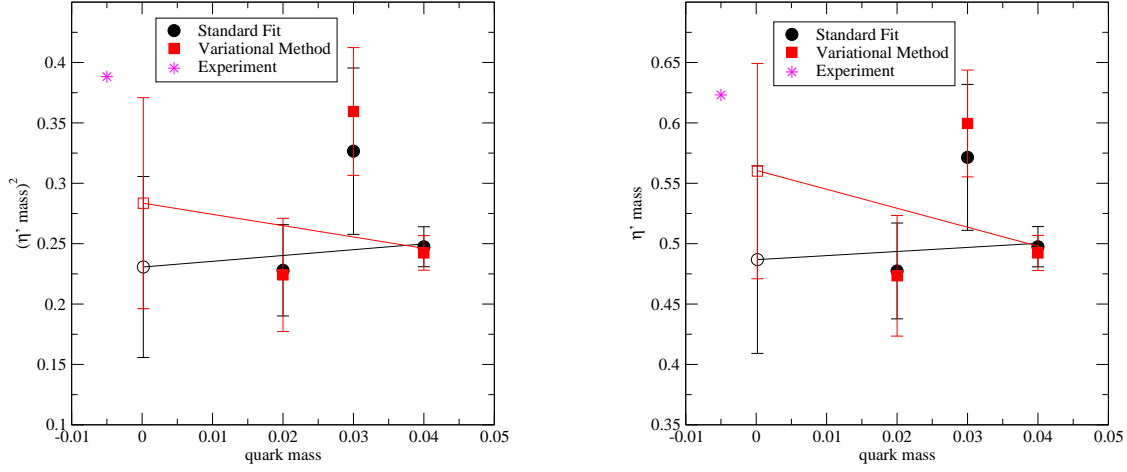


Fig. 11. m_0^2 vs. m_f (left), and m_0 vs. m_f (right). Empty circle and box are extrapolated value at the physical point using (3.65) and (3.66) respectively. The left most star symbols show the experimental value¹⁾ in the real world.

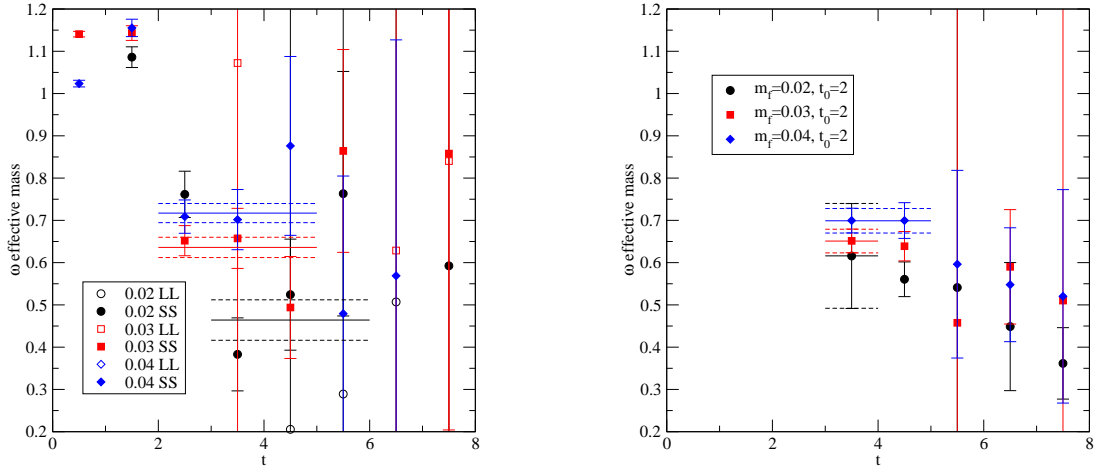


Fig. 12. Effective mass vs. t using method (A) (left) and method (B) (right).

We estimate the extrapolated mass at the physical quark mass point in Figure 13 and Table XI. The formula used is the linear extrapolation (3.66). Since the statistical error on the lightest point $m_f = 0.02$ is so large as mentioned above, our extrapolation is in two folds: using all three masses or the heaviest two points. In Table XI, one could see the

Table X . $m_!$

m_f	$m_!$	t_0	$t_{m \text{ in}}$	$t_{m \text{ ax}}$	m method
0.02	0.464 (48)		3	6	(A)
	0.616 (124)	2	$t_0 + 1$	4	(B)
0.03	0.636 (24)		2	5	(A)
	0.651 (28)	2	$t_0 + 1$	4	(B)
0.04	0.717 (23)		2	5	(A)
	0.699 (29)	2	$t_0 + 1$	5	(B)

results of "m method (A) 3 masses t " is different from that of "m method (A) 2 masses t " significantly. At physical quark mass point, $m_!$ is quoted from "m method (B) 3 masses t ",

$$m_!^{\text{phys}} = 790 (194) \text{ M eV} : \quad (4.7)$$

Our estimation for $!$ turns out to be consistent with the experimental value within large 25 % statistical error.

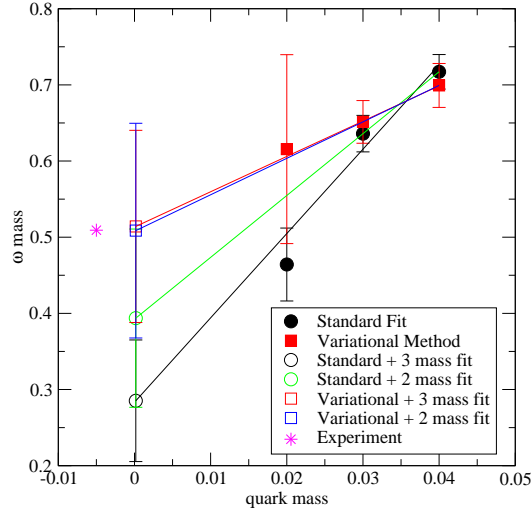


Fig. 13. $m_!$ vs. m_f . The left most star symbol shows the experimental value¹⁾ in the real world.

We also calculate propagators of flavor singlet meson scalar, f_0 using the same quark propagator for 0 and $!$, and found they are too noisy to extract the spectrum at all m_f .

Table XI. m_l estimation at the physical quark mass point ($m_f = m_{u,d}$)

m_l	m_l^{phys} [MeV]	$m_l r_0$	tm method
0.285 (80)	439 (123)	1.22 (34)	(A) 3 masses t
0.394 (117)	605 (180)	1.68 (50)	(A) 2 masses t
0.514 (126)	790 (194)	2.20 (54)	(B) 3 masses t
0.509 (141)	782 (217)	2.18 (60)	(B) 2 masses t

4.6. Pseudovector mesons (a_1, b_1, f_1, h_1) spectrum

Figures 14, 15, 16, and 17 show effective mass using method (A) (left) and method (B) (right), and Tables XII, XIII, XIV, and XV list results of fits for a_1, b_1, f_1, h_1 respectively. Except for h_1 meson propagator at $m_f = 0.03$, the fitting procedure converges.

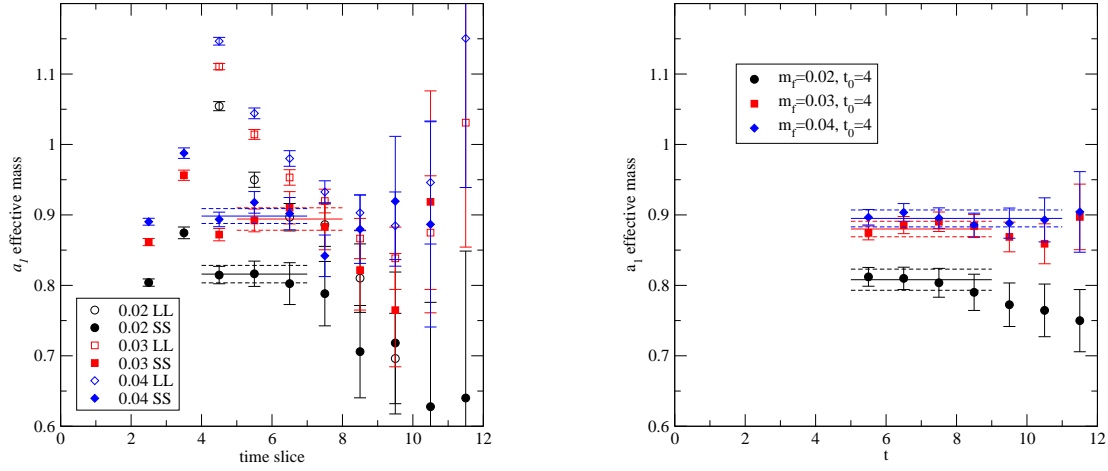


Fig. 14. a_1 effective mass vs. t using method (A) (left) and method (B) (right).

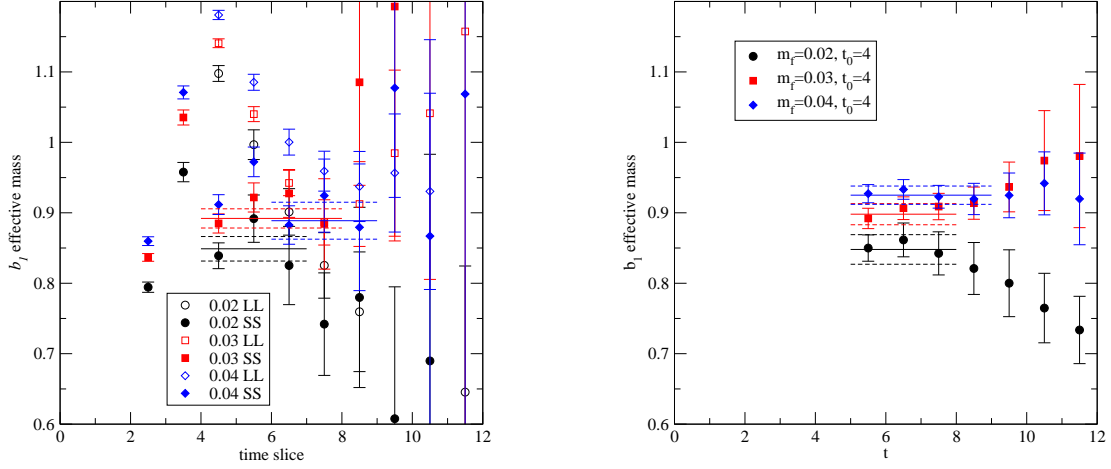


Fig. 15. b_1 effective mass vs. t using method (A) (left) and method (B) (right).

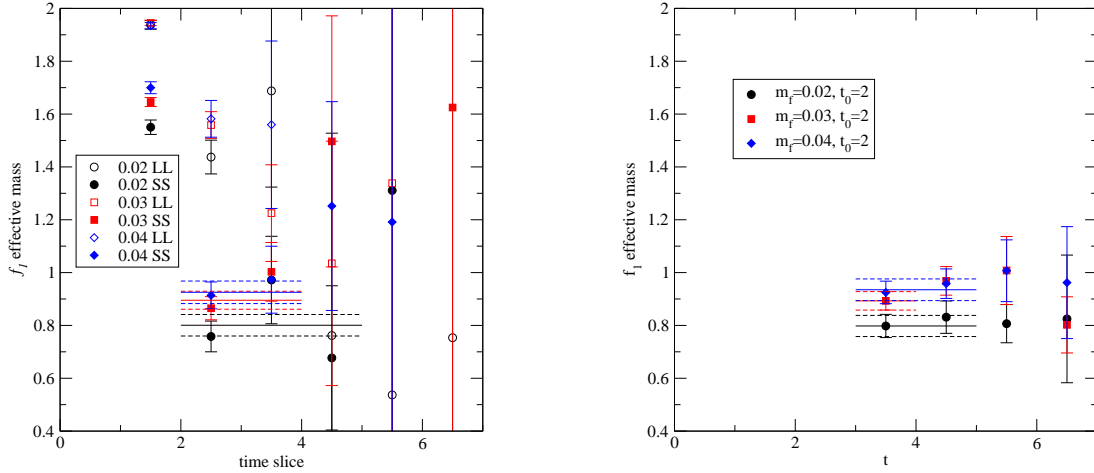


Fig. 16. f_1 effective mass vs. t using method (A) (left) and method (B) (right).

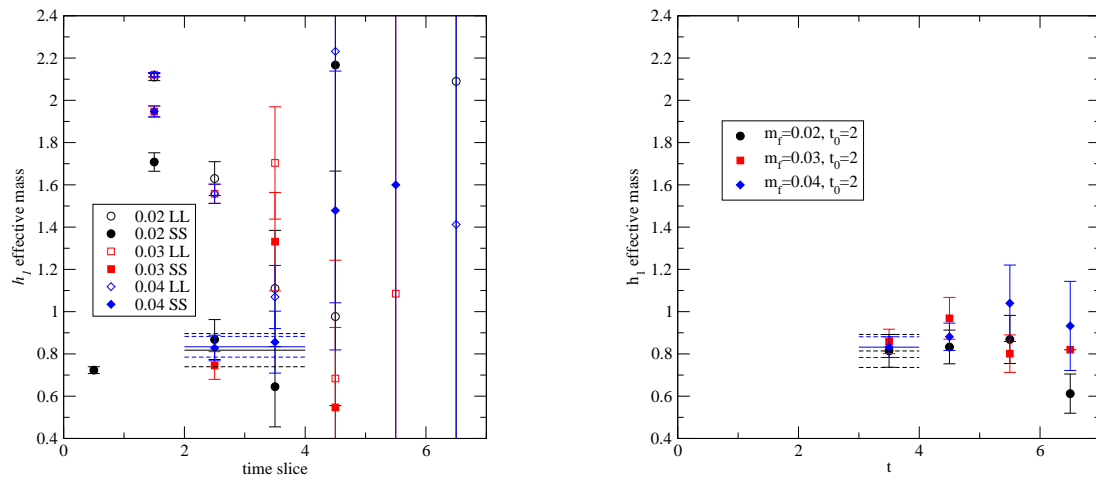


Fig. 17. h_1 effective mass vs. t using method (A) (left) and method (B) (right).

Table X II. m_{a_1}

m_f	m_{a_1}	t_0	$t_{m \text{ in}}$	$t_{m \text{ ax}}$	m ethod
0.02	0.816 (12)		4	7	(A)
	0.808 (15)	4	$t_0 + 1$	9	(B)
0.03	0.894 (16)		5	8	(A)
	0.880 (11)	4	$t_0 + 1$	9	(B)
0.04	0.898 (11)		4	8	(A)
	0.895 (12)	4	$t_0 + 1$	11	(B)

Table X III. m_{b_1}

m_f	m_{b_1}	t_0	$t_{m \text{ in}}$	$t_{m \text{ ax}}$	m ethod
0.02	0.849 (17)		4	7	(A)
	0.848 (21)	4	$t_0 + 1$	8	(B)
0.03	0.892 (14)		4	8	(A)
	0.898 (15)	4	$t_0 + 1$	8	(B)
0.04	0.889 (26)		6	9	(A)
	0.925 (13)	4	$t_0 + 1$	9	(B)

Table X IV . m_{f_1}

m_f	m_{f_1}	t_0	$t_{m \text{ in}}$	$t_{m \text{ ax}}$	m ethod
0.02	0.801 (41)		2	5	(A)
	0.798 (40)	2	$t_0 + 1$	5	(B)
0.03	0.895 (34)		2	4	(A)
	0.893 (35)	2	$t_0 + 1$	4	(B)
0.04	0.925 (43)		2	4	(A)
	0.935 (41)	2	$t_0 + 1$	5	(B)

These meson masses are extrapolated linearly to the physical quark mass point, $m_f = m_{u,d}$, and shown in Figures 18, 19, 20, and 21. The numerical values are summarized in Tables XVI, XVII, XVIII, and XIX for a_1, b_1, f_1, h_1 respectively. As the masses are independent of which methods we chose within statistical error, we choose

$$m_{a_1}^{\text{phys}} = 1.140 (51) \text{ GeV} \quad (4.8)$$

$$m_{b_1}^{\text{phys}} = 1.203 (64) \text{ GeV} \quad (4.9)$$

Table XV . m_{h_1}

m_f	m_{h_1}	t_0	t_{min}	t_{max}	method
0.02	0.818 (78)		2	4	(A)
	0.814 (78)	2	$t_0 + 1$	4	(B)
0.04	0.834 (49)		2	4	(A)
	0.832 (49)	2	$t_0 + 1$	4	(B)

$$m_{f_1}^{\text{phys}} = 1.033 (137) \text{ GeV} \quad (4.10)$$

$$m_{h_1}^{\text{phys}} = 1.225 (250) \text{ GeV} \quad (4.11)$$

from method (B) as our main values.

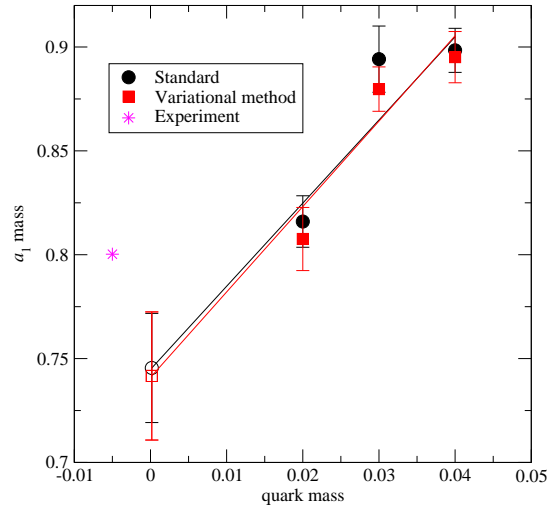


Fig. 18. m_{a_1} vs. m_f . The left most star symbol shows the experimental value¹⁾ in the real world.

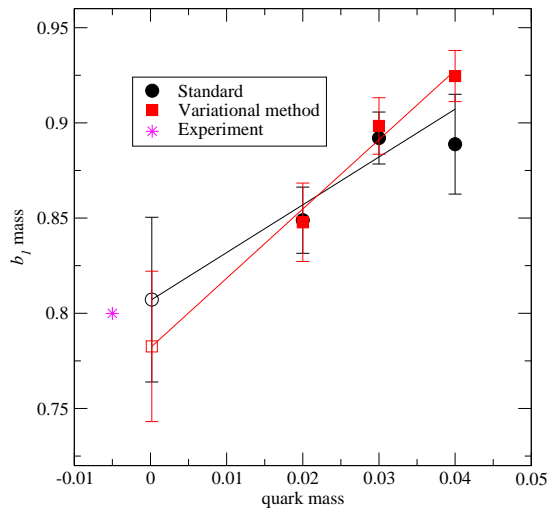


Fig. 19. m_{b_1} vs. m_f . The left most star symbol shows the experimental value¹⁾ in the real world.

These number may be compared with the experimental results for b_1 (1235), h_1 (1170), a_1 (1260) and f_1 (1285), the first two of which are in good agreement with the numerical results. However further investigations based on the realistic settings are clearly needed for more serious comparisons.

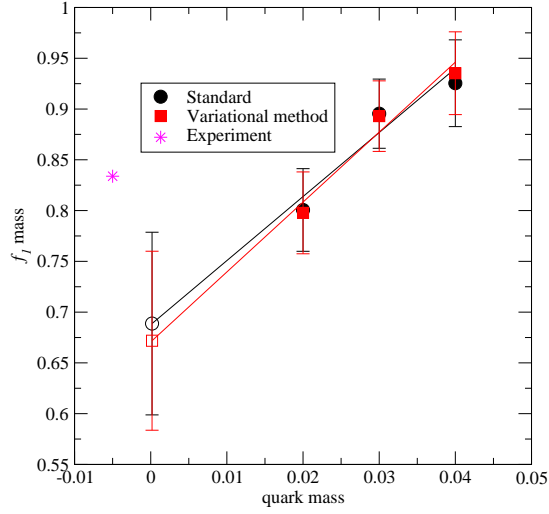


Fig. 20. m_{f_1} vs. m_f . The left most star symbol shows the experimental value¹⁾ in the real world.

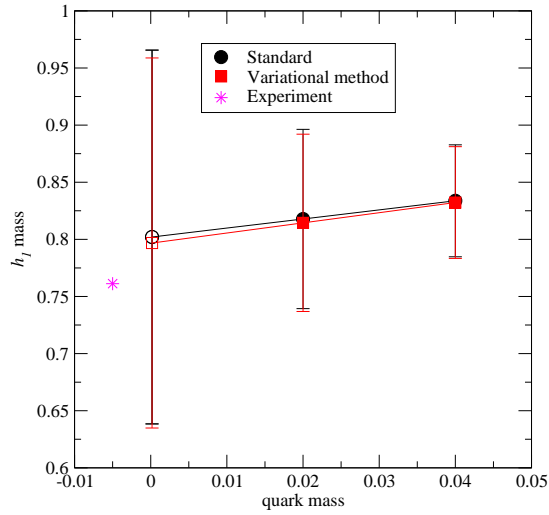


Fig. 21. m_{h_1} vs. m_f . The left most star symbol shows the experimental value¹⁾ in the real world.

4.7. Excited meson (ρ, ω) masses

In this subsection, the second excited states of pion and meson are discussed. In method (B), we extract the eigenvalue for the second excited state, $\rho_0(t); 0 = \dots$; (3.52), which is plotted in right panels of 22 and 23 respectively. Although we only use two variations

Table X V I. m_{a_1} at the physical quark mass point ($m_f = m_{u,d}$)

m_{a_1}	$m_{a_1}^{\text{phys}}$ [M eV]	$m_{a_1} r_0$	method
0.745 (26)	1,146 (45)	3.19 (12)	(A)
0.742 (31)	1,140 (51)	3.17 (14)	(B)

Table X V II. m_{b_1} at the physical quark mass point ($m_f = m_{u,d}$)

m_{b_1}	$m_{b_1}^{\text{phys}}$ [M eV]	$m_{b_1} r_0$	method
0.807 (43)	1,241 (70)	3.45 (19)	(A)
0.783 (40)	1,203 (64)	3.35 (17)	(B)

Table X V III. m_{f_1} at the physical quark mass point ($m_f = m_{u,d}$)

m_{f_1}	$m_{f_1}^{\text{phys}}$ [M eV]	$m_{f_1} r_0$	method
0.689 (90)	1,058 (139)	2.95 (39)	(A)
0.672 (88)	1,033 (137)	2.87 (38)	(B)

Table X V I X . m_{h_1} at the physical quark mass point ($m_f = m_{u,d}$)

m_{h_1}	$m_{h_1}^{\text{phys}}$ [M eV]	$m_{h_1} r_0$	method
0.802 (164)	1,233 (252)	3.43 (70)	(A)
0.797 (162)	1,225 (250)	3.41 (69)	(B)

of operator for each meson, and $\rho(t)$ may have significant contribution from the higher excited state, we explore $\rho(t)$ to extract the temporal exponent, m_ρ , or mass of excited states using the formula (3.54). Results of the fits are shown in Table XX and XXI. We checked the results from $t_0 = 5$ and $t_0 = 6$ are consistent to each other.

Table X X . m_ρ

m_f	m_ρ	t_0	t_{min}	t_{max}	method
0.02	1.215 (50)	5	$t_0 + 1$	8	(B)
0.03	1.211 (27)	5	$t_0 + 1$	8	(B)
0.04	1.242 (26)	5	$t_0 + 1$	8	(B)

We perform linear extrapolation (3.66) to the physical quark mass point, and found

$$m_\rho^{\text{phys}} = 1.791 (138) \text{ GeV} \quad (4.12)$$

$$m_\rho^{\text{phys}} = 2.028 (131) \text{ GeV} \quad (4.13)$$

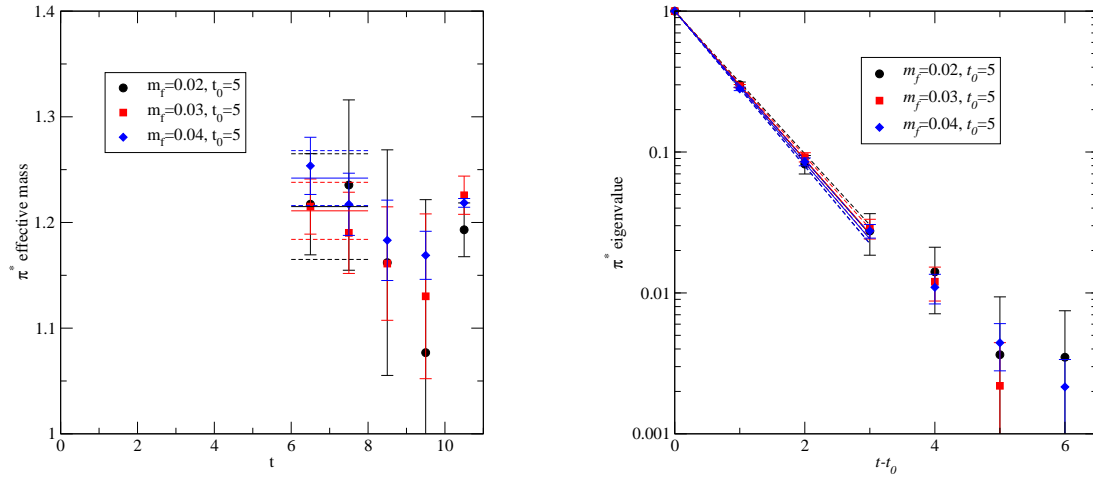


Fig. 22. π 's effective mass and eigenvalue as functions of t and $t - t_0$.

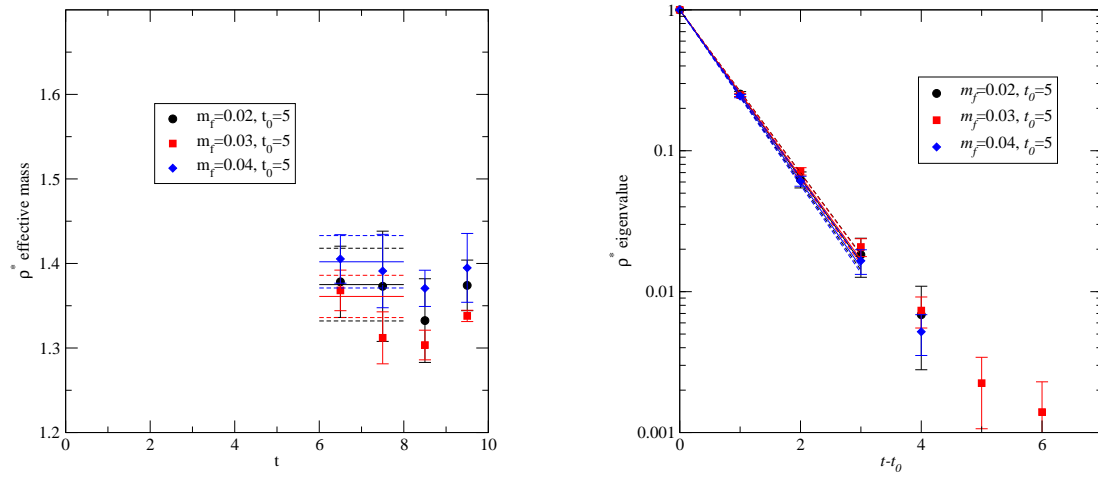


Fig. 23. ρ 's effective mass and eigenvalue as functions of t and $t - t_0$.

(see Table 4.7 and 4.7). These states might be interpreted as (1300) , and (1450) or (1700) .

4.8. Decay constants

As the last subset of numerical results, we present the leptonic decay constant in this subsection. The decay constant of the ground state pion, f_π , is determined using the method (C), fitting the smeared two point function to the formula (3.62). We also do the same

Table XX I. m

m_f	m	t_0	$t_{m_{in}}$	$t_{m_{ax}}$	method
0.02	1.375 (43)	5	$t_0 + 1$	8	(B)
0.03	1.361 (25)	5	$t_0 + 1$	8	(B)
0.04	1.402 (31)	5	$t_0 + 1$	8	(B)

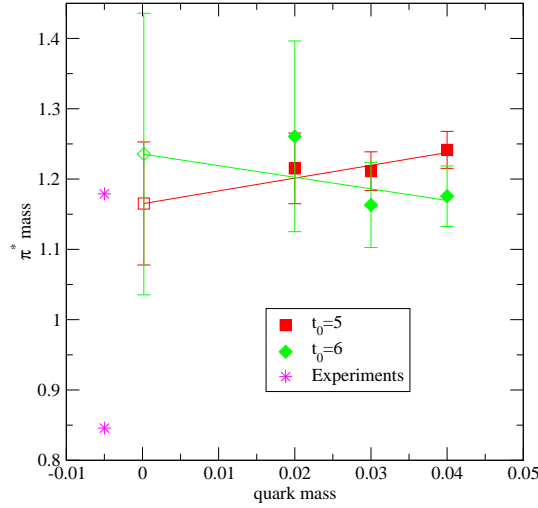


Fig. 24. m vs. m_f . The left most star symbols show the experimental values¹⁾ in the real world.

Table XX II. m at the physical quark mass point ($m_f = m_{u,d}$)

m	m^{phys} [MeV]	m_{r_0}	method
1.165 (88)	1,791 (138)	4.98 (38)	(B)

Table XX III. m at the physical quark mass point ($m_f = m_{u,d}$)

m	m^{phys} [MeV]	m_{r_0}	method
1.319 (82)	2,028 (131)	5.64 (36)	(B)

two point functions to the double exponential formula (3-64) using values of m and m determined from the variational method (method (B)) to explore the decay constant for the second excited state, f , which is called as method (D).

Table XX IV shows the results on each of simulated quark mass. Pion mass and decay constants are consistent to those reported in previous paper²⁴⁾ within statistical error.

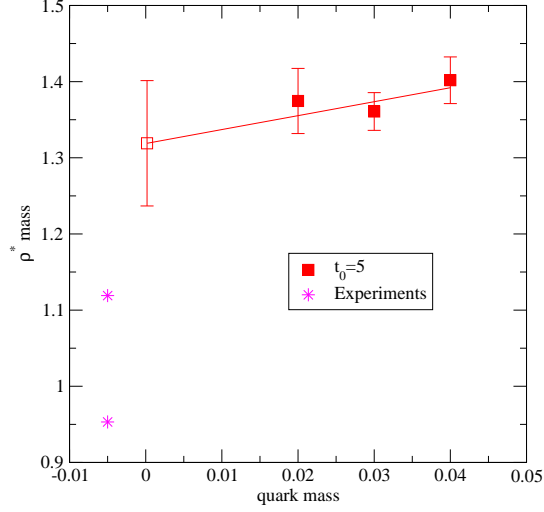


Fig. 25. f_0^* vs. m_f . The left most star symbols show the experimental values¹⁾ in the real world.

Table XXIV. f_0^* and f_0

m_f	m	f_0^*	m	f_0	$t_{m \text{ in}}$	$t_{m \text{ ax}}$	method
0.02	0.2936 (13)	0.09561 (40)			7	14	(C)
	0.2934 (13) (xed)	0.09540 (43)	1.215 (50) (xed)	0.02244 (54)	4	14	(D)
	0.2938 (18) ^a	0.09494 (62) ^a			9	16	(C)
0.03	0.3598 (15)	0.10350 (46)			10	16	(C)
	0.3581 (10) (xed)	0.10370 (44)	1.211 (27) (xed)	0.03236 (65)	4	16	(D)
	0.3610 (18) ^a	0.10253 (56) ^a			9	16	(C)
0.04	0.4098 (12)	0.11002 (39)			8	16	(C)
	0.4092 (11) (xed)	0.10964 (40)	1.242 (26) (xed)	0.04362 (61)	4	16	(D)
	0.4087 (16) ^a	0.11059 (57) ^a			9	16	(C)

(a) These values are quoted in the previous paper.²⁴⁾

Though f_0^* decay constant is numerically poorly determined, it has an interesting theoretical prediction. Axial Ward-Takahashi identity, (3.61), for ρ^0 describe the equation for its decay constant,

$$f_0^* = \frac{2(m_f + m_{\text{res}})}{m^2} \langle 0 | \mathcal{P}^a | j \rangle \quad (4.14)$$

If m_f is not NG boson, so m_f stays non-zero, right hand side vanishes in the chiral limit,

($m_f \neq m_{res}$). This prediction was checked on lattice QCD with Wilson fermions.³⁴⁾ and their f was consistent to be zero at the chiral limit.

Figure 26 and Table XXV show linear extrapolation of f . In the chiral limit, decay constant is also consistent with the theoretical prediction, i.e. $f \neq 0$.

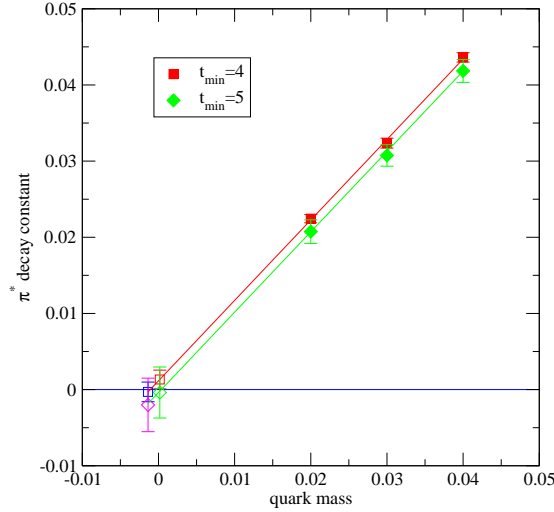


Fig. 26. f vs. m_f .

Table XXV. f at the physical quark mass point ($m_f = m_{u,d}$) and the chiral limit ($m_f = m_{res}$)

m_f	f	f^{phys} [MeV]	f_{r_0}	method
$m_{u,d}$	0.0013 (12)	20 (19)	0.0057 (53)	(D)
m_{res}	0.0003 (13)	05 (20)	0.0013 (57)	(D)

Next we discuss on meson decay constant, f . The result of the fit (3.63) is shown in Table XXVI. meson mass extracted in this fit turns out to be consistent with those from method (A) and (B) within statistical error for all m_f .

Table XXVI. $f = Z_V$

m_f	m	$f = Z_V$	t_{min}	t_{max}	method
0.02	0.5730 (96)	0.2011 (66)	9	13	(C)
0.03	0.6035 (64)	0.2025 (50)	10	14	(C)
0.04	0.6448 (51)	0.2164 (37)	9	14	(C)

Then the decay constant at the physical quark mass point is obtained

$$f^{\text{phys}} = 210(15) \text{ M eV} \quad (4.15)$$

by linear extrapolation. The renormalization factor, Z_V , which converts the lattice operator, into the one in continuum for $\overline{M S}$ at $\mu = 2 \text{ GeV}$ is necessary to obtain a physical value for the decay constants. We use $Z_A = 0.75734(55)$ which was determined in previous paper,²⁴⁾ and the relation $Z_V = Z_A$ relying on the good chiral symmetry of the current simulation.

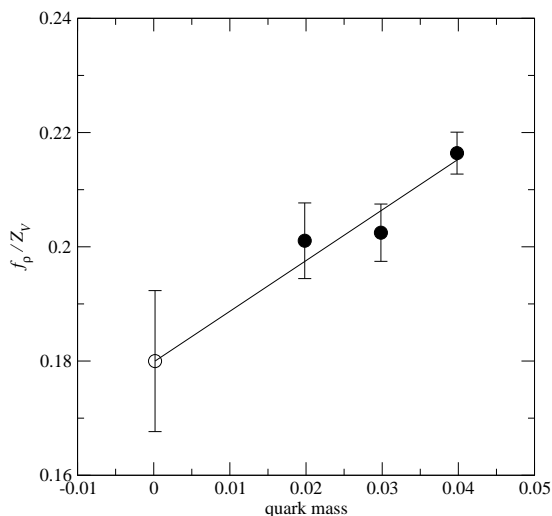


Fig. 27. $f = Z_V$ vs. m_f .

Table XXVII. f at the physical quark mass point ($m_f = m_{u,d}$)

$f = Z_V$	f	$f^{\text{phys}} \text{ [M eV]}$	$f r_0$	method
0.1800(123)	0.1363(94)	210(15)	0.0583(41)	(C)

4.9. Systematic Uncertainties

So far we mainly discussed only about statistical error. Our numerical results are obtained only at one lattice scale, in one space-time volume, for three heavier quark masses than physical ones, and the strange sea quark is neglected. In this section, various sources of systematic error are listed and some of their very rough estimation are discussed to compare our results with experiments.

Approximating the continuous space-time by a discrete lattice costs the discretization error. With DW F it starts with $O(m_{\text{res}} a) + O(a^2 \frac{2}{Q_{CD}})$. The value of $m_{\text{res}} a$ is negligibly

small in our simulation compared to the somewhat large statistical error except for pion. Our results would be closer to their continuum values compared to those with Wilson fermion on similar lattice scale.

For quenched DWF QCD, physical values f , f_K , and $f_K = f$ shift by 5%, 3%, and 2% respectively when lattice scale changes from $a^{-1} = 2 \text{ GeV}$ to continuum limit,³⁵⁾ which are equal or less to current statistical error.

Due to the limited number of quark mass points calculated in our simulation, we restricted ourselves to use the simplest linear chiral extrapolations (3.66) and the one from AW TI (3.65). More appropriate extrapolation with larger number of quark mass points is the one from the (partially quenched) chiral perturbation theory. While π^0 mass explored as a main topic in this work shows little dependence on quark mass, more precise chiral extrapolation to the physical quark mass point using lighter quark masses is needed for more reliable results.

Although the assumption we made, that the ground state is one particle state is certainly wrong for some quantum numbers, some of decay channel in nature are actually prohibited in the simulation with degenerate up and down quark with heavier mass on a relatively small spacial box $(2 \text{ fm})^3$ without strange quark. More sophisticated investigations such as calculating for the scattering amplitudes between multiparticles are needed to check our spectrum results for the decaying meson.

Without larger volume results, it is hard to estimate the finite volume effect although it might be smaller than that for Baryons.

Strange sea quark effect: The number of quark flavors that play dynamical roles in π^0 meson could be very important as seen in the W V relation, m^2_0 / N_f . By increasing N_f from 2 to 3 including strange quark, the W V prediction for m_0 becomes 20% larger. Strange quark is, however, heavier than up/down quarks, and the π^0 mass in $N_f = 2 + 1$ QCD is likely be in between $N_f = 2$ and 3.

Topological charge distribution for π^0 meson: In our simulation, we deliberately use special gauge action, DBW 2, for the good chiral symmetry. In return, the autocorrelation time of topological charge becomes longer.

The samples taken in our simulation may not be not long enough for reliable estimation for auto-correlation time for Q_{top} . The growth of binned-jackknife error for Q_{top} of increasing bin size is monitored, and we estimate the auto-correlation time roughly 300 trajectories for $m_f = 0.02$ ensemble and 200 trajectories at $m_f = 0.03; 0.04$. Having less frequent tunneling between different topological sectors, the charge distribution sampled in our simulation may be statistically skewed. In fact,

D E

$Q_{\text{top}} = 0.7(7); 1.4(6); 1.8(4)$ for $m_f = 0.02; 0.03; 0.04$ respectively. Notice that the central value in $m_f = 0.04$ is more than four sigma away from zero. It is conceivable that this poor sample of topological sectors causes a significant systematic errors in Q_{top} spectrum, especially for $m_f = 0.04$ ensemble.

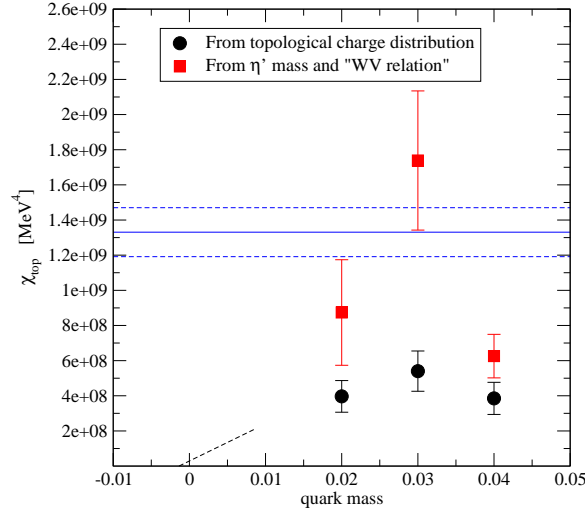


Fig. 28. Circles are measured Q_{top} as a function of m_f ^{(24), (52)} while boxes are calculated from $m_{\eta'}$ and m_{sea} as described in the next section. Horizontal line is the value from pure SU(3) Yang-Mills simulation. ⁽⁴⁾ Dotted line is prediction from chiral perturbation theory.

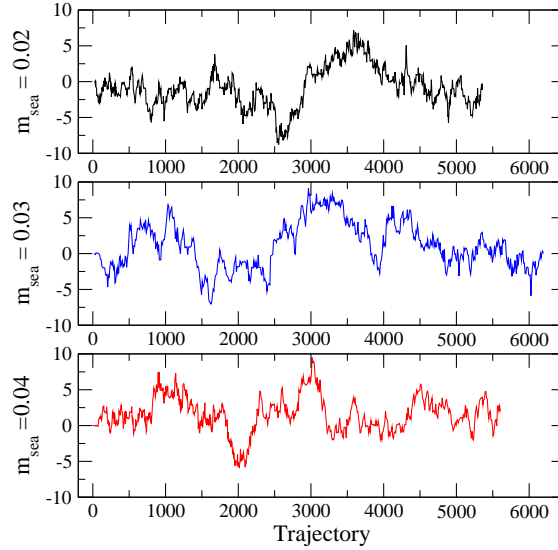


Fig. 29. History of the topological charge in simulation based on same as Figure 28.

Figure 28 shows the topological susceptibility, χ_{top} in (1.4) as a function of quark mass. The fact the susceptibility at all three masses are constant within two sigma implies that the simulation points are far from the lighter quark mass region, where the susceptibility may vanish linearly in quark masses. It is also possible the tunneling between different topological sectors occurs not enough frequently, as seen in Figure 29, so that the estimation for the susceptibility has larger systematic error.

Of course, more reliable check for these systematic errors could be estimated by future simulations on finer and larger lattice using lighter quark masses with strange sea quark effect with higher statistics.

5. Summary and Discussions

We have measured light mesons in all channel (flavor non-singlet/singlet pseudoscalar, vector, scalar, pseudovector and tensor meson $\rho, \omega, a_0, a_1, b_1; \eta, \eta', f_0, f_1, h_1$) propagators and estimated the ground state meson masses and some of leptonic decay constants, as well as, the excited state mass, in two flavors of domain wall QCD.

Statistic of our calculation is increased by five to ten times compared to the one reported previously.²⁴⁾ By applying the gauge invariant smearing ala Wuppertal for quark operators for their better overlap to the ground state, the statistical error of pion and η is reduced by approximately 50% and the reduction for η' is more than 100%, i.e. we were only able to obtain the non-zero signal in the data with smearing. To extract values for meson mass and decay constant by fitting the propagators, we use two methods, the standard and the variational methods. Results of these methods are consistent with each other, which indicates the excited state contamination to the ground state is under control thanks to the smearing.

Systematic uncertainties discussed in the previous section are difficult to estimate, so that we quote our results only with statistical errors. Our results linearly extrapolated to the physical quark mass point are

$$a_m^{-1} = 1.537(26) \text{ GeV}$$

$$r_0 = 0.5491(93) \text{ fm}$$

for quantities directly related to the lattice scale,

$$f_\pi = 210(15) \text{ MeV}$$

$$f_\eta = 20(19) \text{ MeV}$$

for decay constants, and

$$\begin{aligned}
m_{a_0} &= 1.111(81) \text{ GeV} \\
m_{\pi^0} &= 819(127) \text{ MeV} \\
m_{\eta} &= 790(194) \text{ MeV} \\
m_{\rho} &= 1.791(138) \text{ GeV} \\
m_{\omega} &= 2.028(131) \text{ GeV} \\
m_{a_1} &= 1.140(51) \text{ GeV} \\
m_{b_1} &= 1.203(64) \text{ GeV} \\
m_{f_1} &= 1.033(137) \text{ GeV} \\
m_{h_1} &= 1.225(250) \text{ GeV} ;
\end{aligned}$$

for mass spectrum. The lattice scale is set from $m_{\pi^0} = 775.49 \text{ MeV}$.

In Figure 30, the meson masses carried out in this work are compared to the experimental values¹⁾ in the real world. Horizontal bars are the experimental values and filled circles show the simulation results. The error bars indicate statistical error only.

The decay constant of the excited pseudoscalar meson turns out to be consistent with zero at the chiral limit as expected:

$$f_{\pi^0} = 0.05(20) \text{ MeV} \quad (5.1)$$

The flavor singlet scalar meson, f_0 , was too noisy to get the mass in our data.

In this paper we chose the simplest noise method, complex Z_2 , in evaluating the quark loop amplitudes. More elaborated and/or sophisticated methods³⁶⁾⁽⁴⁰⁾ could improve the statistical accuracy of the calculation.

Recalculated pion is consistent to previous result, but results for ρ and a_0 meson masses are significantly changed. The central value of m_{ρ} is 10% larger, i.e. a_m^{-1} is 10% smaller, and the error bar is reduced by 50% compared to the previous results.²⁴⁾ Both the central value and error bar of m_{a_0} become 25% smaller than previous results.²⁵⁾

We confirm that the flavor singlet pseudoscalar meson, π^0 , would not be NG boson, m_{π^0} is not likely zero in the chiral limit, which is consistent with the standard understanding of axial anomaly. Assuming WV relation (1.3) is exact at $N_c = 3$, one could calculate the mass gap, m_0^2 , and topological susceptibility, χ_{top} , from our values of m_{π^0} and m_{ρ} :

$$\chi_{\text{top}}(WV) = \frac{f^2}{2N_f} m_0^2; \quad m_0^2 = m_{\rho}^2 - m_{\pi^0}^2 \quad (5.2)$$

Nf=2 DWF at $a^{-1}=1.5 \text{ GeV}$ on $(2.1 \text{ fm})^3$

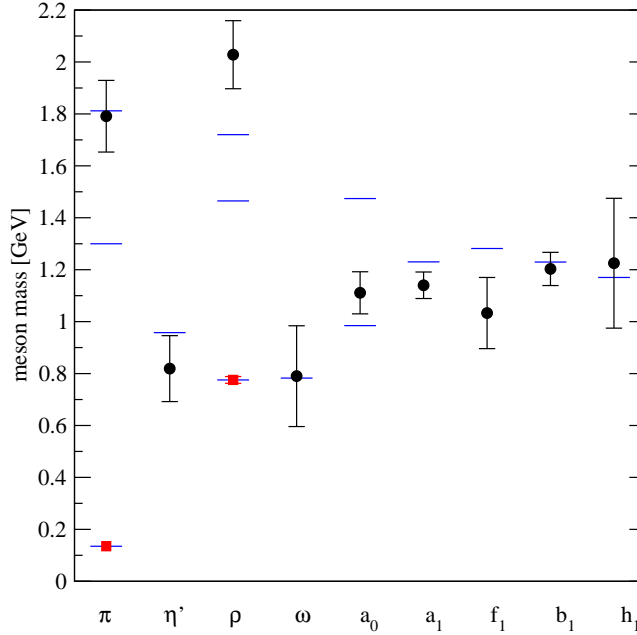


Fig. 30. Comparison of simulation results with experimental values¹⁾ in the real world. Horizontal bars are the experimental values and filled circles show the simulation results. The error bars indicate statistical error only. The boxes are the quantities used to set the lattice spacing and the physical quark mass point.

$m_{\text{top}}(W, V)$ for $N_f = 2$ are plotted in Figure 28 as box symbols. Horizontal line is the m_{top} from pure SU(3) Yang-Mills simulation.⁴⁾ For $m_f = 0.02; 0.03$, $m_{\text{top}}(W, V)$ is consistent with quenched value while $m_f = 0.04$ point under shoot the quenched value significantly. By linearly extrapolations to the chiral limit, we found $m_0^2 = (808(129) \text{ MeV})^2$ and $m_{\text{top}}(W, V) = (193(15) \text{ MeV})^4$, which turns out to be consistent with the quenched value⁴⁾ $(191(5) \text{ MeV})^4$. The agreement, which implies small $1=N_c$ correction, is interesting, and deserves further investigations in future.

These results are susceptible to various systematic errors. First of all, we only have two flavors of dynamical quarks. The omission of strange quark and anti-quark pairs in vacuum, whose mass is comparable to the dynamical scale of QCD, may skew our results significantly. The limited number of quark mass, three unitary points, restricted us to examine other than the simplest function for the quark mass dependence of physical results. Thus the chiral extrapolation has systematic error due to the ignored curvature from the chiral logarithms and higher order terms though many of our results show little dependence on quark mass. The ensemble were generated only on $16^3 \times 32$ lattice with periodic boundary condition in space directions thus all the meson spectrum has effects from their "mirror" images placed at

2 fm away from the original in age in every three spacial directions. The effects may be as savour as 10 % level especially for lightest quark mass points. The lattice discretization used in this study is O(a) improved modulus all m_{res} effects. The previous careful studies²⁴⁾ for the scaling violation show 5% level shift for a 0:1 fm lattices. The omission of isospin violation due to the differences of quark mass and electric charge are likely ignorable compared to other sources of errors, but this issue can also be studied non-perturbatively on lattice.²⁹⁾ Despite of the significant statistical error and the various systematic uncertainties remaining, this study should serve a benchmark calculation for statistical feature of the difficult observable, disconnected diagrams, and computational feasibility test. The results of 0 mass turned out to be close to the experimental 0 mass, which encourages further improvements especially calculation on $N_f = 2 + 1$ DW F ensemble.^{32),33)}

Acknowledgements

We thank RIKEN, Brookhaven National Laboratory and U.S. Department of Energy for providing the facilities essential for the completion of this work. We are grateful to members of the RBC collaboration, especially to T. Blum, N. Christ, C. Dawson, R. Mawhinney, K. Orginos, and A. Soni for their various contributions at early stage of this work and continuous encouragements. The QCD0C supercomputer at the RIKEN-BNL Research Center (RBRC) was used for the numerical calculations in this work. K.H. thanks RBRC for its hospitality where this work was performed. We are grateful for authors and maintainers of CPS,⁵³⁾ which are used in this work. This work is supported in part by Grants-in-Aid for Scientific Research from the Ministry of Education, Culture, Sports, Science and Technology (No. 17750050).

References

- 1) W. M. Yao et al. [Particle Data Group], *J. Phys. G* **33**, 1 (2006).
- 2) E. Witten, *Nucl. Phys. B* **156**, 269 (1979).
- 3) G. Veneziano, *Nucl. Phys. B* **159**, 213 (1979).
- 4) L. DelDebbio, L. Giusti and C. Pica, *Phys. Rev. Lett.* **94**, 032003 (2005) [arXiv:hep-th/0407052].
- 5) S. Itoh, Y. Iwasaki and T. Yoshie, *Phys. Rev. D* **36**, 527 (1987).
- 6) Y. Kuramashi, M. Fukugita, H. Mino, M. Okawa and A. Ukawa, *Phys. Rev. Lett.* **72**, 3448 (1994).
- 7) M. Fukugita, Y. Kuramashi, M. Okawa and A. Ukawa, *Phys. Rev. D* **51**, 3952 (1995).
- 8) V. I. Lesk et al. [CP-PACS Collaboration], *Phys. Rev. D* **67**, 074503 (2003)

- [arXiv:hep-lat/0211040].
- 9) C. M. d'Neile and C. Michael [UKQCD Collaboration], Phys. Lett. B 491, 123 (2000) [Erratum -ibid. B 551, 391 (2003)] [arXiv:hep-lat/0006020].
 - 10) C. R. Allton et al. [UKQCD Collaboration], Phys. Rev. D 70, 014501 (2004) [arXiv:hep-lat/0403007].
 - 11) T. Stuckmann et al. [TXL Collaboration], Phys. Rev. D 63, 074503 (2001) [arXiv:hep-lat/0010005].
 - 12) K. Schilling, H. Ne and T. Lippert, Lect. Notes Phys. 663, 147 (2005) [arXiv:hep-lat/0401005].
 - 13) S. Aoki et al. [JLQCD Collaborations], PoS LAT 2006, 204 (2006) [arXiv:hep-lat/0610021].
 - 14) L. Venkataraman and G. Kilcup, arXiv:hep-lat/9711006.
 - 15) E. B. Gregory, A. C. Irving, C. M. Richards and C. M d'Neile, PoS LAT 2006, 176 (2006) [arXiv:hep-lat/0610044].
 - 16) S. R. Sharpe, PoS LAT 2006, 022 (2006) [arXiv:hep-lat/0610094].
 - 17) M. Creutz, arXiv:0708.1295 [hep-lat].
 - 18) D. B. Kaplan, Phys. Lett. B 288, 342 (1992) [arXiv:hep-lat/9206013].
 - 19) Y. Shamir, Nucl. Phys. B 406, 90 (1993) [arXiv:hep-lat/9303005].
 - 20) V. Furman and Y. Shamir, Nucl. Phys. B 439, 54 (1995) [arXiv:hep-lat/9405004].
 - 21) T. Takaishi, Phys. Rev. D 54, 1050 (1996).
 - 22) P. de Forcrand et al. [QCD-TARO Collaboration], Nucl. Phys. B 577, 263 (2000) [arXiv:hep-lat/9911033].
 - 23) Y. Aoki et al., Phys. Rev. D 69, 074504 (2004) [arXiv:hep-lat/0211023].
 - 24) Y. Aoki et al., Phys. Rev. D 72, 114505 (2005) [arXiv:hep-lat/0411006].
 - 25) S. Prelovsek, C. Dawson, T. Izubuchi, K. Orginos and A. Soni, Phys. Rev. D 70, 094503 (2004) [arXiv:hep-lat/0407037].
 - 26) S. Gusken, Nucl. Phys. Proc. Suppl. 17, 361 (1990).
 - 27) C. Michael, Nucl. Phys. B 259, 58 (1985).
 - 28) M. Luscher and U. Wol, Nucl. Phys. B 339, 222 (1990).
 - 29) T. Blum, T. Doi, M. Hayakawa, T. Izubuchi and N. Yamada, arXiv:0708.0484 [hep-lat].
 - 30) V. Gadiyak and O. Lofkvik, Phys. Rev. D 72, 114504 (2005) [arXiv:hep-lat/0509075].
 - 31) C. Dawson, T. Izubuchi, T. Kaneko, S. Sasaki and A. Soni, Phys. Rev. D 74, 114502 (2006) [arXiv:hep-ph/0607162].
 - 32) D. J. Antonio et al. [RBC and UKQCD Collaborations], Phys. Rev. D 75, 114501 (2007) [arXiv:hep-lat/0612005].

- 33) C. Allton et al. [RBC and UKQCD Collaborations], *Phys. Rev. D* 76, 014504 (2007) [[arXiv:hep-lat/0701013](#)].
- 34) C. M. d'Neile and C. Michael [UKQCD Collaboration], *Phys. Lett. B* 642, 244 (2006) [[arXiv:hep-lat/0607032](#)].
- 35) Y. Aoki et al., *Phys. Rev. D* 73, 094507 (2006) [[arXiv:hep-lat/0508011](#)].
- 36) J. Foley, K. Jimmy Juge, A. O'Cais, M. Peardon, S. M. Ryan and J. I. Skullerud, *Comput. Phys. Commun.* 172, 145 (2005) [[arXiv:hep-lat/0505023](#)].
- 37) A. Duncan and E. Eichten, *Phys. Rev. D* 65, 114502 (2002) [[arXiv:hep-lat/0112028](#)].
- 38) T. A. DeGrand and S. Schaefer, *Comput. Phys. Commun.* 159, 185 (2004) [[arXiv:hep-lat/0401011](#)].
- 39) C. Michael and J. Peisa [UKQCD Collaboration], *Phys. Rev. D* 58, 034506 (1998) [[arXiv:hep-lat/9802015](#)].
- 40) S. Collins, G. Bali and A. Schafer, [arXiv:0709.3217 \[hep-lat\]](#).
- 41) C. M. d'Neile and C. Michael [UKQCD Collaboration], *Phys. Rev. D* 74, 014508 (2006) [[arXiv:hep-lat/0604009](#)].
- 42) K. F. Liu, *Prog. Theor. Phys. Suppl.* 168, 160 (2007) [[arXiv:0706.1262 \[hep-ph\]](#)].
- 43) A. Hart, C. M. d'Neile and C. Michael [UKQCD Collaboration], *Nucl. Phys. Proc. Suppl.* 119, 266 (2003) [[arXiv:hep-lat/0209063](#)].
- 44) T. Burch, C. Gattringer, L. Y. Glozman, C. Hagen, C. B. Lang and A. Schafer, *Phys. Rev. D* 73, 094505 (2006) [[arXiv:hep-lat/0601026](#)].
- 45) W. A. Bardeen, A. Duncan, E. Eichten, N. Isgur and H. Thacker, *Phys. Rev. D* 65, 014509 (2001) [[arXiv:hep-lat/0106008](#)].
- 46) E. B. Gregory, A. C. Irving, C. M. Richards and C. M. d'Neile, [arXiv:0709.4224 \[hep-lat\]](#).
- 47) E. B. Gregory, A. Irving, C. M. Richards, C. M. d'Neile and A. Hart, [arXiv:0710.1725 \[hep-lat\]](#).
- 48) C. Michael and C. Urbach [ETM Collaboration], *PoS LAT2007*, 122 (2007) [[arXiv:0709.4564 \[hep-lat\]](#)].
- 49) T. Izubuchi, S. Aoki, K. Hashimoto, Y. Nakamura, T. Sekido and G. Schierholz, *PoS LAT2007*, 106 (2007) [[arXiv:0802.1470 \[hep-lat\]](#)].
- 50) Y. Shamir, *Nucl. Phys. B* 417, 167 (1994) [[arXiv:hep-lat/9310006](#)].
- 51) T. Blum et al., *Phys. Rev. D* 66, 014504 (2002) [[arXiv:hep-lat/0102005](#)].
- 52) F. Berruto, T. Blum, K. Orginos and A. Soni, *Phys. Rev. D* 73, 054509 (2006) [[arXiv:hep-lat/0512004](#)].
- 53) <http://qcdoc.phys.columbia.edu/~chulwoo/index.html>